

**Hyperbolic decoupling of tangent space and effective dimension of dissipative systems**Kazumasa A. Takeuchi,<sup>1,2</sup> Hong-liu Yang,<sup>3</sup> Francesco Ginelli,<sup>1,4,5,6</sup> Günter Radons,<sup>3</sup> and Hugues Chaté<sup>1</sup><sup>1</sup>*Service de Physique de l'État Condensé, CEA-Saclay, F-91191 Gif-sur-Yvette, France*<sup>2</sup>*Department of Physics, The University of Tokyo, 7-3-1 Hongo, Bunkyo-ku, Tokyo 113-0033, Japan*<sup>3</sup>*Institute of Physics, Chemnitz University of Technology, D-09107 Chemnitz, Germany*<sup>4</sup>*Istituto dei Sistemi Complessi (ISC), CNR, Via dei Taurini 19, I-00185 Roma, Italy*<sup>5</sup>*Physics Department, University of Florence, Via Sansone 1, I-50019 Sesto Fiorentino, Italy*<sup>6</sup>*Department of Physics and SUPA, University of Aberdeen, Aberdeen AB24 3UE, United Kingdom*

(Received 13 July 2011; published 25 October 2011)

We show, using covariant Lyapunov vectors, that the tangent space of spatially extended dissipative systems is split into two hyperbolically decoupled subspaces: one comprising a finite number of frequently entangled “physical” modes, which carry the physically relevant information of the trajectory, and a residual set of strongly decaying “spurious” modes. The decoupling of the physical and spurious subspaces is defined by the absence of tangencies between them and found to take place generally; we find evidence in partial differential equations in one and two spatial dimensions and even in lattices of coupled maps or oscillators. We conjecture that the physical modes may constitute a local linear description of the inertial manifold at any point in the global attractor.

DOI: [10.1103/PhysRevE.84.046214](https://doi.org/10.1103/PhysRevE.84.046214)

PACS number(s): 05.45.–a, 05.70.Ln, 05.90.+m, 02.30.Jr

**I. INTRODUCTION**

Nonlinear, dissipative, partial differential equations (PDEs) are frequently used for describing natural phenomena in all fields of physics and beyond. They are particularly important for out-of-equilibrium problems such as pattern formation, turbulence, spatiotemporal chaos, etc. [1,2]. Because of the nonlinearities involved, their generic solutions are mostly studied via numerical simulation.

A simple question arises then: Can one faithfully integrate such PDEs, which are formally infinite-dimensional dynamical systems, when numerical schemes obviously involve only a finite number of degrees of freedom? For the practitioner, the answer is yes, as one easily observes that with increasing numerical resolution the obtained (chaotic) solutions converge in the sense that they exhibit the same dynamical or statistical properties. Mathematically speaking, the notion of inertial manifold, on which all trajectories evolve after a short transient, is crucial in this context [3–5]. For generic parabolic PDEs such as the Kuramoto-Sivashinsky (KS) equation [2] and the complex Ginzburg-Landau (CGL) equation [6], it is in fact proven that trajectories are first exponentially attracted to a finite-dimensional inertial manifold and eventually settle in a global attractor of finite Hausdorff dimension [7–11]. The inertial manifold is a smooth object embedding the global attractor, which in principle reduces the evolution of trajectories to a finite set of ordinary differential equations. However, this mathematical object remains largely formal, for lack of a constructive way to determine which modes actually constitute it.

In fact, even the dimension of the minimal inertial manifold stays beyond the reach of mathematical arguments. So far, only upper bounds have been calculated, such as  $L^{2.46}$  for the one-dimensional KS equation in a domain of size  $L$  [8,9]. This is to be contrasted with the intuitive expectation that it should grow linearly with  $L$ , as suggested by the extensivity of chaos [12] observed routinely in generic one-dimensional systems [13–17] including the KS equation [13,14].

In a different context, Cvitanović and co-workers have developed a constructive approach to unravel the “skeleton” of the chaotic dynamics of dissipative systems including PDEs [18–20]: By exploiting hierarchies of unstable periodic orbits, chaotic solutions are represented rather faithfully in simplified, finite-dimensional spaces, and some quantitative properties can be systematically estimated. However, it is not clear how the finite-dimensional inertial manifold can emerge from the interplay of infinitely many unstable periodic orbits involved, to various degrees, in the dynamics.

In the present paper, we show results that could constitute a first step toward a constructive approach to the finite-dimensional inertial manifold of dissipative PDEs. Using Lyapunov analysis, we study the tangent-space evolution of spatially extended dynamical systems. Since  $N$ -dimensional dynamical systems have  $N$  Lyapunov exponents, the numerical integration of a given PDE provides as many Lyapunov exponents as one likes by just increasing the spatial resolution. Now, suppose that this PDE has an inertial manifold of finite dimension and that we use a resolution with a larger number of degrees of freedom. In a recent work [21], we showed that covariant Lyapunov vectors, which span the Oseledec subspaces [22] and give the intrinsic directions of growth of perturbations for each Lyapunov exponent, exhibit a decomposition of tangent space into a fixed, finite number of “physical” modes and a remaining set of “spurious” modes, whose number increases with increasing resolution. The excess spurious modes are associated with very negative Lyapunov exponents and “hyperbolically” decoupled from the physical modes. Hence, perturbations along them quickly decay and do not spread to any physical mode. Below, we pursue this approach and provide a precise characterization of the decoupling between the physical and spurious modes. We show in particular that the decoupling takes place even between arbitrary combinations of physical or spurious modes, defining a finite-dimensional manifold in the tangent space, which should contain all the relevant information for the phase-space dynamics. We also provide a criterion giving an

accurate estimate of the dimension of the physical manifold from finite-time simulations.

As mentioned above, the key quantities to access this hyperbolic decoupling are covariant Lyapunov vectors (CLVs). At each point in phase space, they constitute the intrinsic directions of growth of perturbations associated with each Lyapunov exponent; in other words, they span the Oseledec subspaces [22]. Therefore, their spatial structure is meaningful and their relative angles rule the hyperbolicity properties of the dynamical system. Note that they *cannot* be replaced, even qualitatively, by the Gram-Schmidt vectors, which are by-products of the standard method [23,24] to compute Lyapunov exponents. It is only recently that CLVs have become rather easy to compute numerically, notably thanks to the efficient algorithm presented in Ref. [25]. In the present study, we compute the Lyapunov exponents by the standard Gram-Schmidt method [23,24] and the associated CLVs by Ginelli's algorithm [25].

The paper is organized as follows. In Sec. II, we demonstrate our main results using the one-dimensional (1D) KS equation, a prototypical dissipative PDE showing spatiotemporal chaos. We then apply the same approach to the 1D CGL equation in Sec. III to show how the hyperbolic decoupling reflects phase-space dynamics in different regimes of spatiotemporal chaos. In particular, we study what is called the phase turbulence regime [6] of the CGL equation, in order to answer the long-standing question regarding whether this regime can be fully described by “phase modes.” In Secs. IV and V we study 1D lattice systems and the 2D KS equation, respectively, demonstrating the general existence of the physical manifold. Section VI contains a discussion and our conclusions.

## II. 1D KURAMOTO-SIVASHINSKY EQUATION

### A. Definition and numerical scheme

We first focus on the 1D KS equation [1,2]:

$$\frac{\partial u}{\partial t} = -\frac{\partial^2 u}{\partial x^2} - \frac{\partial^4 u}{\partial x^4} - u \frac{\partial u}{\partial x}, \quad x \in [0, L], \quad (1)$$

with a real-valued field  $u(x, t)$ . Boundary conditions are set to be periodic (PBC)  $u(x, t) = u(x + L, t)$  for most of the data below, but rigid boundary conditions (RBC)  $u(0, t) = u(L, t) = 0$  are also used for comparison. The size is fixed at  $L = 96$  unless otherwise indicated, for which the 1D KS equation exhibits spatiotemporal chaos with both boundary conditions. For numerical integration, we use the pseudospectral method with discrete Fourier or sine modes up to a cutoff wave number  $k_{\text{cut}}$ . The number of collocation points is chosen so that no aliasing may occur. Integration is carried out with the operator-splitting method, which adopts the second-order Adams-Moulton method for the linear terms and Heun's method (two-stage second-order Runge-Kutta method) for the nonlinear term, with time step 0.005. Most of the data presented in this section are obtained with PBC,  $L = 96$ , and  $k_{\text{cut}} = 42 \times 2\pi/L$ , that is, with 43 Fourier modes, from integration over a period of roughly  $10^5$  after a transient period about  $10^4$  is discarded.

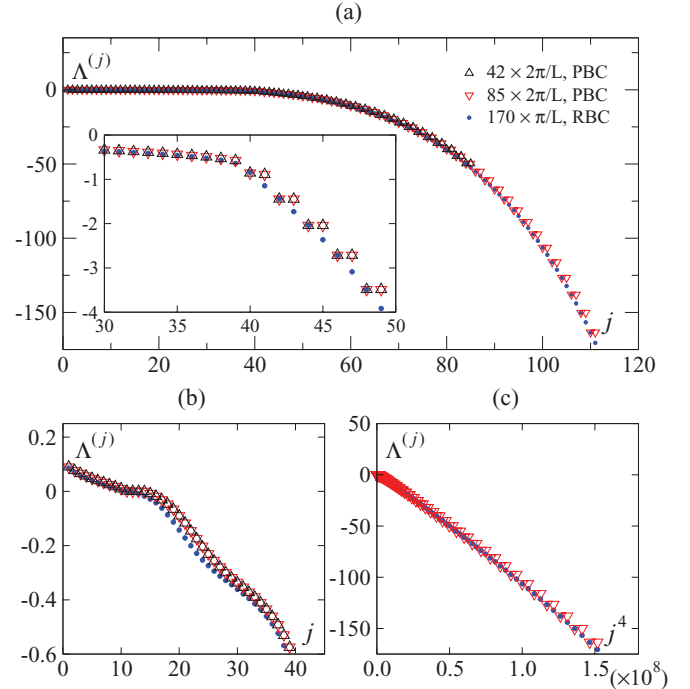


FIG. 1. (Color online) Spectrum of the Lyapunov exponents  $\Lambda^{(j)}$  for the 1D KS equation with  $L = 96$ . (a) Full spectra. Different symbols correspond to different cutoff wave numbers  $k_{\text{cut}}$  and different boundary conditions, either PBC or RBC, as indicated in the legend. (Inset) Close-up around the threshold. (b) Close-up of (a) showing the positive end of the spectra. (c) The same Lyapunov spectra shown against  $j^4$ . The data for  $k_{\text{cut}} = 42 \times 2\pi/L$  with PBC (black upward triangles) are omitted for the sake of clarity. The value of the Kaplan-Yorke dimension is about 21.6 for  $k_{\text{cut}} = 42 \times 2\pi/L$  and PBC.

### B. Lyapunov exponents and Lyapunov vectors

Figures 1(a) and 1(b) show the spectrum of the Lyapunov exponents  $\Lambda^{(j)}$  arranged in descending order for different spatial resolutions and boundary conditions. The Lyapunov spectrum consists of two parts: first, a smooth region of positive, zero, and negative exponents and, second, a rather steep region of negative exponents arranged in steps of two for PBC. The two regions are separated by an abrupt change in slope, accompanied by the formation of a stepwise structure for PBC (inset). Remarkably, the spectra for different spatial resolutions overlap almost perfectly, with additional exponents due to the improved resolution simply accumulating at the negative end of the second region (upward and downward triangles). Thus, the threshold separating the two regions remains unchanged (here around  $j = 40$ ) upon increasing the resolution, though its exact index cannot be defined unambiguously only from the spectrum and will be given later on a firm basis. Note also that in the second region the boundary conditions only change the multiplicity of modes: Every other mode overlaps nicely for both types of boundary conditions. All these observations lead to a speculation that the Lyapunov modes in the second region are “spurious” and dampen quickly, whereas all the physical properties of the dynamics are carried by the Lyapunov modes in the first region. This intuition shall be substantiated in the following

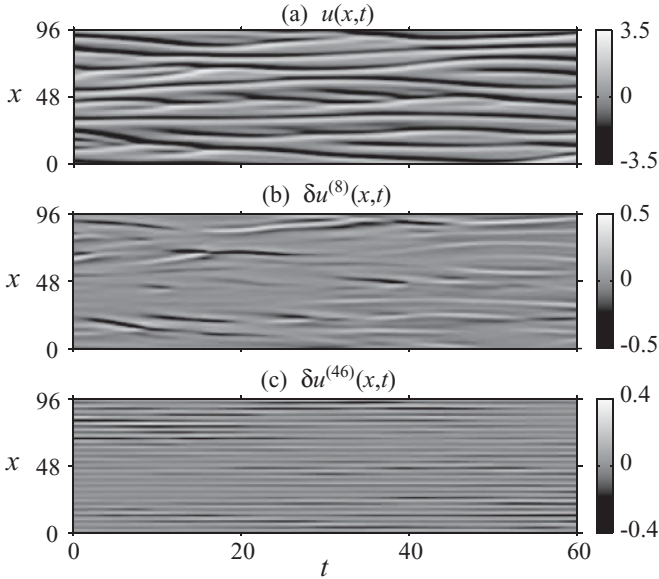


FIG. 2. Typical spatiotemporal structure of the trajectory  $u(x,t)$  (a) and CLVs  $\delta u^{(j)}(x,t)$  (b), (c) in the physical and the spurious regions, respectively, for the 1D KS equation ( $L = 96$ ,  $k_{\text{cut}} = 42 \times 2\pi/L$ , PBC). The index of the CLV shown here is  $j = 8$  (b) and  $j = 46$  (c).

by studying the CLVs  $\delta u^{(j)}(x,t)$  associated with the Lyapunov exponents  $\Lambda^{(j)}$ .

Figure 2 shows typical spatiotemporal structures of CLVs in the physical and the spurious regions of the Lyapunov spectrum as well as that of the trajectory for the resolution  $k_{\text{cut}} = 42 \times 2\pi/L$  with PBC (corresponding to the black upward triangles in Fig. 1). At first glance, the CLVs for the physical and spurious Lyapunov modes have qualitatively different structures; whereas CLVs of the physical modes [Fig. 2(b)] evolve in a manner similar to the trajectory itself [Fig. 2(a)], those of the spurious modes are essentially sinusoidal apart from a slight modulation of the amplitude [Fig. 2(c)]. This can be seen more clearly in the spatial power spectra of the CLVs [Fig. 3(a)]. In contrast to the smooth structure of the spectra found for the physical modes, those for the spurious modes are characterized by the existence of a sharp peak for the sinusoidal structure, whose wave number  $k_{\text{peak}}^{(j)}$  increases

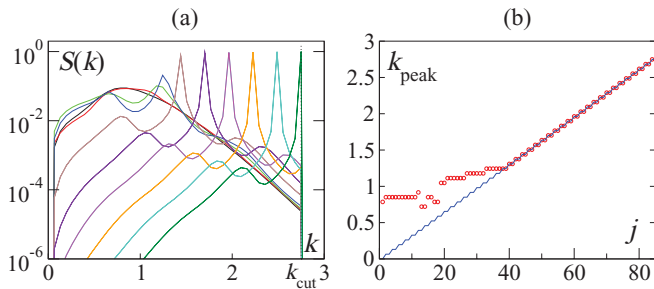


FIG. 3. (Color online) Spatial power spectrum of the CLVs for the 1D KS equation ( $L = 96$ ,  $k_{\text{cut}} = 42 \times 2\pi/L$ , PBC). (a) Power spectrum of CLVs of index  $j = 1, 16, 32, 38, 44, 52, 60, 68, 76$ , and  $84$  (from left to right at the peak positions). (b) Peak wave number  $k_{\text{peak}}$  of the power spectra (red circles) and  $k = [j/2] \times 2\pi/L$  (blue line).

linearly with the index  $j$  [Fig. 3(b)]. For PBC, the two modes forming a step in the Lyapunov spectrum are found to have the same peak wave number and even the same power spectrum, but with an arbitrary phase shift in the vector structure. This multiplicity of two does not exist with RBC, since the phase of the sinusoid is fixed at the boundary. Moreover, the peak wave number  $k_{\text{peak}}^{(j)}$  turns out to be simply the  $j$ th wave number, with the multiplicity taken into account, allowed in the given spatial geometry:  $k_{\text{peak}}^{(j)} = [j/2] \times 2\pi/L$  for PBC [Fig. 3(b)], where  $[x]$  is the integer part of  $x$ . The power spectra of the spurious modes [Fig. 3(a)] show that they are dominated by a sinusoidal structure at this trivial wave number  $k_{\text{peak}}^{(j)}$ , and even more so as  $j$  is large. Therefore, the value of their Lyapunov exponent is determined predominantly by the stabilizing linear term of the KS equation, that is, the fourth-order derivative, and hence  $\Lambda^{(j)} \approx -(k_{\text{peak}}^{(j)})^4 \sim -j^4$  for large enough  $j$ , as is indeed confirmed in Fig. 1(c).

### C. Angles between covariant Lyapunov vectors

The sinusoidal structure of the Lyapunov vectors of spurious modes suggests that they are nearly orthogonal to each other. Unlike Gram-Schmidt vectors, CLVs allow us to check this directly through the angle  $\theta^{(i,j)}$  between vectors defined by the inner product

$$\cos \theta^{(i,j)}(t) \equiv \int_0^L \delta u^{(i)}(x,t) \delta u^{(j)}(x,t) dx, \quad (2)$$

with  $L^2$ -normalized vectors  $\int_0^L \delta u^{(i)}(x,t)^2 dx = 1$ . Since the angle  $\theta$  fluctuates in time, one needs to study its distribution function  $\rho_v(\theta)$ .

The result is shown in Fig. 4(a) for PBC. Indeed, the angle distributions  $\rho_v(\theta)$  between any pairs of CLVs of index  $j \geq 42$  are peaked at  $\pi/2$  and drop rapidly near  $0$  and  $\pi$  [pairs (41,42), (43,44), and (61,62) in Fig. 4(a)]. This is also true if one of the vectors is taken in the region  $j \leq 41$  [pair (20,60)], but when both vectors are taken from this region [pairs (39,40) and (40,41)], the angle distribution spans the whole  $[0, \pi]$  interval. The change in the distribution is found to be quite sharp in this example; notice that the indices are varied only one by one for neighboring pairs in Fig. 4(a) [the pairs in the same step, e.g., (42,43), are skipped]. The transition between physical and spurious modes can thus be characterized by the existence or the absence of vector tangencies, arbitrarily close to the phase-space trajectory. An angle distribution bounded away from  $0$  and  $\pi$  marks the absence of such tangencies, while a finite weight at  $0$  or  $\pi$  indicates that the given pair of vectors has a finite probability of forming any arbitrarily small angle along the phase-space trajectory. Note that while two different, nondegenerate CLVs, will never be exactly coincident, thus tangent, at any point of the phase-space trajectory, they can get arbitrarily close to each other if the angle distribution has a finite value at  $0$  or  $\pi$ . In the following, we use the term tangency to describe this latter occurrence. With this in mind, the results in Fig. 4(a) show that the physical modes exhibit such tangencies rather frequently. In contrast, the spurious modes, in addition to the negative values of their Lyapunov exponent, do not have any tangencies with other spurious modes (except the partner in the same step) nor with physical

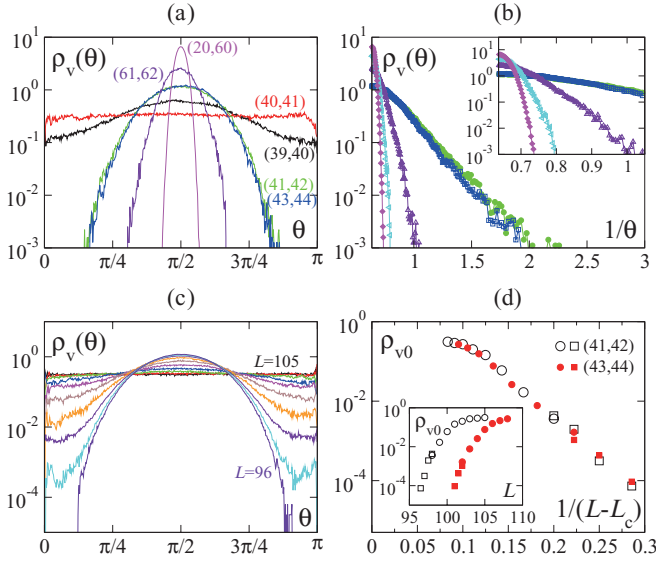


FIG. 4. (Color online) Distributions  $\rho_v(\theta)$  of the angles  $\theta$  between pairs of CLVs for the 1D KS equation ( $k_{\text{cut}} = 42 \times 2\pi/L$ , PBC). (a)  $\rho_v(\theta)$  versus  $\theta$  for  $L = 96$ . The indices of the pairs are indicated on the figure. (b)  $\rho_v(\theta)$  versus  $1/\theta$  for  $L = 96$  and for pairs (41,42), (43,44), (61,62), (81,82), (20,60) from right to left. The ordinate is averaged over both sides of the distribution. (Inset) Close-up of the distributions. (c) Angle distributions  $\rho_v(\theta)$  for the pair (41,42) with varying system size  $L = 96, 97, \dots, 105$  (from inside to outside in the figure). The distribution is obtained from shorter simulations for  $L > 99$ , recorded over time  $10^5$ . (d) Probability density  $\rho_{v0}$  of the distribution  $\rho_v(\theta)$  at  $\theta = 0$  and  $\pi$ , as a function of  $L$  (inset) and of  $1/(L - L_c)$  with a given  $L_c$  (main panel). Pairs of the vectors are fixed at (41,42) (black open symbols) and (43,44) (red full symbols). The value of  $L_c$  is  $L_c = 93.0$  for the pair (41,42) and  $L_c = 97.5$  for (43,44). The circles and squares correspond to the recording times  $10^5$  and  $10^6$ , respectively.

modes. In this sense, they are hyperbolically isolated from any other modes.

A closer look reveals that, while at the threshold index the tail of the angle distribution decreases as  $\rho_v(\theta) \sim \exp(-\text{const}/\theta)$  with decreasing  $\theta$  within our numerical precision, showing an essential singularity at  $\theta = 0$  and  $\pi$ , it decays even more rapidly for larger indices [Fig. 4(b)]. This qualitative change of behavior provides, in our opinion, a more accurate way of defining the threshold. Nevertheless, care should be taken when arguing about the existence or the absence of tangencies from finite-time simulations. To determine the exact threshold, one needs to perform a careful asymptotic analysis on the frequency of tangencies. This can be achieved by studying the system size dependence of the angle distribution  $\rho_v(\theta)$ . Figure 4(c) shows how  $\rho_v(\theta)$  changes for a given pair of CLVs, the pair (41,42) here, with varying system size  $L$ . The value of  $\rho_v(\theta)$  at the tail, denoted by  $\rho_{v0}$ , decreases with decreasing  $L$ , and from a certain system size the tail disappears [inset of Fig. 4(d)]. A singularity analysis shows that it decays as  $\rho_{v0} \sim \exp[-\text{const}/(L - L_c)]$ , providing a threshold  $L_c = 93$  for the pair (41,42) and  $L_c = 97.5$  for (43,44) [main panel of Fig. 4(d)]. This, in turn, allows us to determine the exact number of the threshold index, or the number of the physical modes, at  $N_{\text{ph}} = 43$  for  $L = 96$ . The

critical decay of the angle distribution observed for a fixed size  $L$ ,  $\rho_v(\theta) \sim \exp(-\text{const}/\theta)$ , remains up to  $\theta \rightarrow 0$ , strictly, only at  $L = L_c$  for a given pair of indices; otherwise, it should be eventually replaced by a faster decay or convergence to a finite value.

Be aware that the threshold  $N_{\text{ph}}$  determined here does *not* coincide with the index at which the stepwise structure of the Lyapunov spectrum is formed for PBC [ $j = 40$  here; see inset of Fig. 1(a)]. Indeed, a closer scrutiny of the exponents reveals that the first few steps are actually slightly inclined, and hence no threshold can be unambiguously defined from them. The exponents alone can only provide a good guess of the location of the threshold; instead, it must be determined from the hyperbolicity properties, as evidenced in this section.

#### D. Angles between subspaces

In the previous section we showed the hyperbolic decoupling of all the spurious modes from any physical mode. This, however, does not necessarily imply that they are also decoupled from the manifold spanned by the physical modes, as properly pointed out by Kuptsov and Kuznetsov [26], since it does not exclude the possibility of tangencies between a linear combination of physical modes and of spurious ones. Here, following the idea in Ref. [26], we clarify this issue by studying the smallest possible angle formed by any linear combination of physical modes and any linear combination of spurious modes. It is equivalent to the minimum angle between the subspaces spanned by them.

The angle between subspaces can be computed as follows: Given the matrices  $Q_{\text{ph}}$  and  $Q_{\text{sp}}$  defining the orthogonal bases of the two subspaces, which can be easily obtained by the QR decomposition of the arrays of the corresponding CLVs, the minimum angle between the two subspaces can be obtained simply from the singular value decomposition of the matrix  $Q_{\text{ph}}^T Q_{\text{sp}}$  [27,28], as

$$\cos \phi = \sigma_1(Q_{\text{ph}}^T Q_{\text{sp}}), \quad (3)$$

where  $\sigma_1$  is the largest singular value and the superscript  $T$  denotes the transpose [29].

Figure 5 shows the result, which does not change the view presented above. The angle distribution  $\rho_s(\phi)$  is bounded away from zero [Fig. 5(a)], so that no tangency exists even between the two subspaces. The tail of the distribution is governed by the pairs of Lyapunov modes of closest indices from both groups, and hence we find a similar critical decay  $\rho_s(\phi) \sim \exp(-\text{const}/\phi)$  within the observed time window (inset). The system size dependence is also studied in the same manner [Fig. 5(b)], providing the same value of  $L_c$  as from the vector angle distribution  $\rho_v(\theta)$  shown in Fig. 4(d). This implies that the subspace spanned by the  $N_{\text{ph}}$  physical modes is hyperbolically decoupled from the subspace of the remaining spurious modes or from any other single spurious mode. In strong contrast, inside the manifold of the physical Lyapunov modes, these modes are highly entangled with frequent tangencies as we have found in Fig. 4(a).

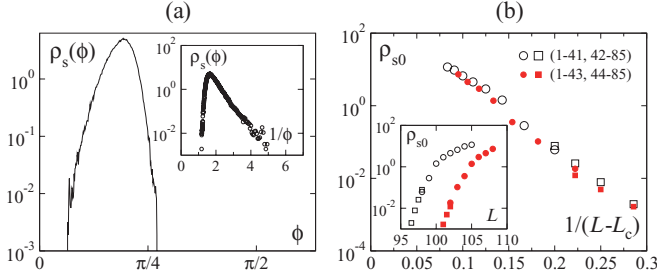


FIG. 5. (Color online) Distribution  $\rho_s(\phi)$  of the angle  $\phi$  between the physical and spurious subspaces for the 1D KS equation ( $k_{\text{cut}} = 42 \times 2\pi/L$ , PBC). (a)  $\rho_s(\phi)$  versus  $\phi$  for  $L = 96$ . The physical subspace is spanned by CLVs of index 1 to  $N_{\text{ph}} = 43$ , while the rest spans the spurious subspace. Note that  $\phi$  is by definition equal to or smaller than  $\pi/2$ , in contrast to  $\theta$  in Fig. 4. (Inset) The same data shown against  $1/\phi$ . (b) Probability density  $\rho_{s0}$  of the distribution  $\rho_s(\theta)$  at  $\phi = 0$  for varying system size  $L$ . It is measured between two subspaces spanned by CLVs of indices given in the legend, and shown against  $L$  (inset) and  $1/(L - L_c)$  (main panel) with the same  $L_c$  as in Fig. 4(d). The circles and squares correspond to the recording times  $10^5$  and  $10^6$ , respectively.

### E. Domination of Oseledec splitting

The absence of tangencies for the spurious modes can also be confirmed from another viewpoint, specifically, in terms of the domination of the Oseledec splitting (DOS) [30,31]. Roughly, DOS refers to the dynamical isolation of the Oseledec subspaces from each other due to the strict ordering of the local expansion rates. Let  $\lambda_\tau^{(j)}(t)$  be the finite-time Lyapunov exponent obtained by averaging the local expansion rate of the  $j$ th CLV from time  $t$  to  $t + \tau$ , that is,

$$\lambda_\tau^{(j)}(t) \equiv \frac{1}{\tau} \log \|J_\tau(t) \delta u^{(j)}(x, t)\|, \quad (4)$$

where  $J_\tau(t)$  is the Jacobian operator for the evolution of the given dynamical system over time  $\tau$  and the CLVs are normalized as  $\|\delta u^{(j)}(x, t)\|^2 \equiv \int_0^L \delta u^{(j)}(x, t)^2 dx = 1$ . Then, the splitting of a pair of 1D subspaces, or CLVs, of indices  $j_1$  and  $j_2 (> j_1)$  is said to be dominating if  $\lambda_\tau^{(j_1)}(t) > \lambda_\tau^{(j_2)}(t)$  holds for all  $t$  with  $\tau$  larger than a finite  $\tau_0$ . It has been mathematically proven that DOS indicates the absence of tangency between the corresponding CLVs [30,31]. To quantify DOS, we define, following [32]

$$\Delta \lambda_\tau^{(j_1, j_2)}(t) \equiv \lambda_\tau^{(j_1)}(t) - \lambda_\tau^{(j_2)}(t). \quad (5)$$

We then measure the time fraction of the DOS violation

$$v_\tau^{(j_1, j_2)} = \langle 1 - \Theta[\Delta \lambda_\tau^{(j_1, j_2)}(t)] \rangle, \quad (6)$$

where  $\Theta(z)$  is the step function and the brackets denote the time average. Note that one needs to compute the finite-time Lyapunov exponents  $\lambda_\tau^{(j)}(t)$  from the CLVs, *not* from the standard method based on the QR decomposition [23,24], because they indicate different local expansion rates despite the same values of the long-time average. The right ones reflecting the physical properties of the tangent space, such as DOS, are those from the CLVs [30,31].

The result is shown in Fig. 6. The DOS violation fraction  $v_\tau^{(j, j+1)}$  for the pairs of the neighboring exponents with  $\tau = 0.2$

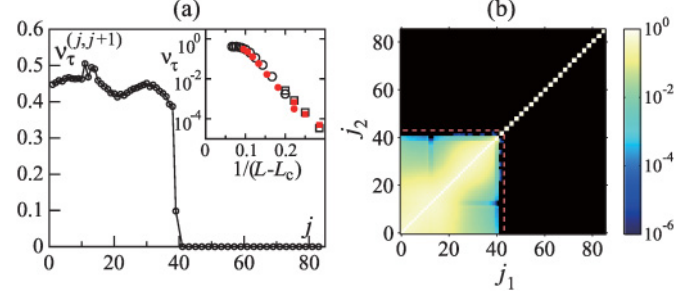


FIG. 6. (Color online) Violation of DOS in the KS equation ( $L = 96$ ,  $k_{\text{cut}} = 42 \times 2\pi/L$ , PBC). (a) Time fraction of the DOS violation,  $v_\tau^{(j, j+1)}$ , for pairs of the neighboring modes with  $\tau = 0.2$ . The pairs within the same step are omitted. (Inset)  $v_\tau^{(j, j+1)}$  with  $j = 41$  (black open symbols) and  $j = 43$  (red solid symbols), shown against  $1/(L - L_c)$  with the same  $L_c$  as in Fig. 4(d). The circles and squares correspond to the recording times  $10^5$  and  $10^6$ , respectively. (b)  $v_\tau^{(j_1, j_2)}$  for arbitrary pairs. The black color indicates  $v_\tau^{(j_1, j_2)} = 0$ , that is, hyperbolically isolated pairs. The red dashed lines indicate the threshold  $N_{\text{ph}} = 43$  between the physical and spurious modes.

drops sharply near the threshold and becomes strictly zero for  $j \geq N_{\text{ph}} = 43$  [Fig. 6(a)] except the pairs in the same step. This split is found not only for the pairs of the neighbors; in fact,  $v_\tau^{(j_1, j_2)}$  stays zero for any pair that includes a spurious mode [Fig. 6(b)], as expected from the fact that all the spurious modes are hyperbolically decoupled from the physical modes. The exact number of the physical modes  $N_{\text{ph}}$  can also be checked from the system size dependence of  $v_\tau^{(j, j+1)}$  [inset of Fig. 6(a)] in the same way as for the angle distributions of the vectors or the subspaces. All this confirms the absence of tangencies of the spurious modes, which has already been seen from the angle distributions, indicating the same number of the physical modes.

### F. What does the absence of tangencies imply?

We now explore the implication of the absence of tangencies for the spurious modes. Suppose that we add an infinitesimal perturbation along an arbitrary CLV to the dynamics. If this is a spurious mode, the perturbation decays exponentially to zero, as indicated by their negative Lyapunov exponents. Further, the absence of tangencies implies that this does not induce any perturbation along the directions spanned by the other Lyapunov modes. In contrast, perturbations along the physical modes will propagate to other physical modes through the tangencies between them, that is, whenever two modes get arbitrarily close to each other, and eventually induce activity in all the physical modes. This is true even if the initial perturbation was made along the physical modes with negative exponents, since they are directly or indirectly connected to those with positive exponents, where the propagated perturbation exponentially grows to affect the phase-space dynamics considerably. The situation does not change if we initially add a perturbation along a linear combination of physical or spurious CLVs: Since the physical and spurious subspaces themselves are hyperbolically isolated (Fig. 5), activities in the spurious modes decay altogether without propagating to one or a set of physical modes, and vice versa. In this sense, the dynamics

corresponding to the physical modes is highly entangled, but completely decoupled from the decaying dynamics of the spurious modes.

Moreover, we find that the number of the physical modes  $N_{\text{ph}}$  does not depend on the spatial resolution, provided it is high enough. This implies that even in the high resolution limit, or in the original PDE, the number of the physical modes remains the same, while infinitely many spurious modes can appear by increasing the resolution. Therefore, the physical modes are probably associated with the finite number of the intrinsic degrees of freedom describing the dynamics of the PDE. This leads to the conjecture that the physical modes may span the local linear approximation of the (minimal) inertial manifold. The number of the physical modes  $N_{\text{ph}}$  would then indicate the inertial manifold dimension, which is the smallest possible number of degrees of freedom to describe the dynamics of the given system.

### G. Extensivity

The physical modes being the active degrees of freedom of the system, one expects that their number  $N_{\text{ph}}$  scales linearly with the system size  $L$  in systems known otherwise to show extensive chaos. This is indeed the case: In Fig. 7 the Lyapunov spectra with their index rescaled by  $L$  collapse both in the physical and in the spurious regions with the stepwise structure retained. As suggested from this collapse, the number of physical modes is found to increase linearly with  $L$ ; that is, it is an extensive quantity, just like the other common quantities indicating effective dimensions of a dynamical system [22] such as the number of the non-negative Lyapunov exponents and the Kaplan-Yorke dimension (inset of Fig. 7). Note that the physical manifold dimension  $N_{\text{ph}}$  (blue triangles) is the largest, in particular, larger than the Kaplan-Yorke dimension (red squares). This corroborates the speculation made above that the physical manifold may provide a tangent-space representation of the inertial manifold,

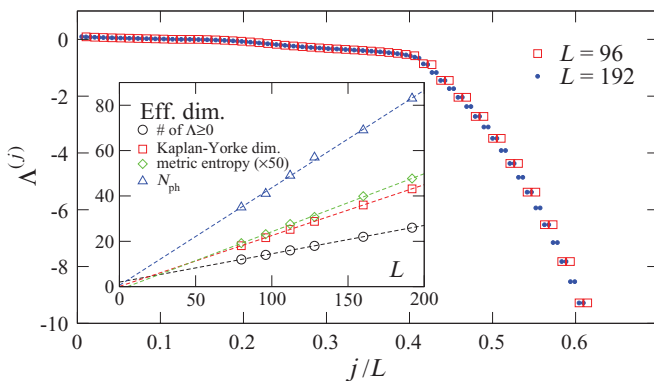


FIG. 7. (Color online) Extensivity of the Lyapunov spectrum (main panel) and effective dimensions (inset) of the KS equation (with PBC). Shown in the inset are the number of the non-negative Lyapunov exponents (black circles), the Kaplan-Yorke dimension (red squares), the metric entropy (green diamonds, multiplied by 50), and the number of the physical modes  $N_{\text{ph}}$  (blue triangles).  $N_{\text{ph}}$  is estimated here from finite-time simulations of given sizes, so that it could be slightly underestimated. The dashed line indicates linear regression for each quantity.

which is a smooth manifold embedding the global attractor. Though, clearly, some mathematical rigor is needed here, our result may provide an estimate of the KS inertial manifold dimension  $D$  at

$$D = N_{\text{ph}} \approx 0.43 \times L, \quad (7)$$

which is drastically lower than the existing mathematical upper bound  $D \leq \text{const} \times L^{2.46}$  [8,9]. Given the length scale  $2\pi\sqrt{2}$  associated with the most unstable wave number of the KS equation, which can be taken as the size of the “building blocks” of spatiotemporal chaos in this system, the above estimate implies that each building block contains roughly  $2\pi\sqrt{2} \times 0.43 \approx 3.8$  degrees of freedom.

In fact, the estimate in Eq. (7) is obtained from the angle distributions and the DOS violation of finite-time simulations, so that the prefactor in Eq. (7) may be slightly underestimated. If we use, instead, the fact that  $N_{\text{ph}}$  increases exactly by two between two threshold sizes  $L_c = 93.0$  and  $97.5$ , we obtain  $N_{\text{ph}} \approx 0.44 \times L$ , or 4.0 physical modes per building block of length  $2\pi\sqrt{2}$ . This estimate is remarkably close to the result of an argument by Sasa [33] showing that solutions of the 1D KS equation can be reconstructed, at least qualitatively, with four modes per building block.

## III. 1D COMPLEX GINZBURG-LANDAU EQUATION

### A. Definition and numerical scheme

To elucidate the generality of our finding, we now consider the CGL equation. It describes oscillatory modulations in spatially extended continuous media at the most basic level, but the genericity of the phenomena described by the CGL equation is known to be, in fact, much larger [1,6]. In one spatial dimension, it governs a complex field  $W(x,t)$  with  $x \in [0, L]$  according to

$$\frac{\partial W}{\partial t} = W - (1 + i\beta)|W|^2 W + (1 + i\alpha)\frac{\partial^2 W}{\partial x^2}, \quad (8)$$

for which the phase  $\Phi(x,t)$  associated with the isochrone [2] of the local oscillation is given by

$$\Phi(x,t) = \arg W(x,t) - \beta \ln |W(x,t)|. \quad (9)$$

We consider here only PBC,  $W(x+L,t) = W(x,t)$ . Numerical integration is performed similarly to the KS equation, with the pseudospectral method and the operator-splitting method implemented by the second-order Adams-Moulton and Heun’s methods. The time step is set to be 0.01.

We study here two representative regimes of the spatiotemporal chaos of the CGL equation, namely the amplitude turbulence regime and the phase turbulence regime [6,34,35]. Both regimes correspond to the situation where plane-wave solutions are rendered unstable by the Benjamin-Feir instability. When varying the parameter values and crossing the Benjamin-Feir line at  $\alpha\beta = -1$ , one first encounters the phase turbulence regime; the phase field  $\Phi(x,t)$  controls the spatiotemporal chaos, while the amplitude  $|W(x,t)|$  remains rather quiescent, staying nonzero everywhere [Fig. 8(a)]. Beyond this regime, amplitude turbulence takes place, in which defects associated with null amplitude and discontinuous change in the phase, in other words, phase slips, are constantly

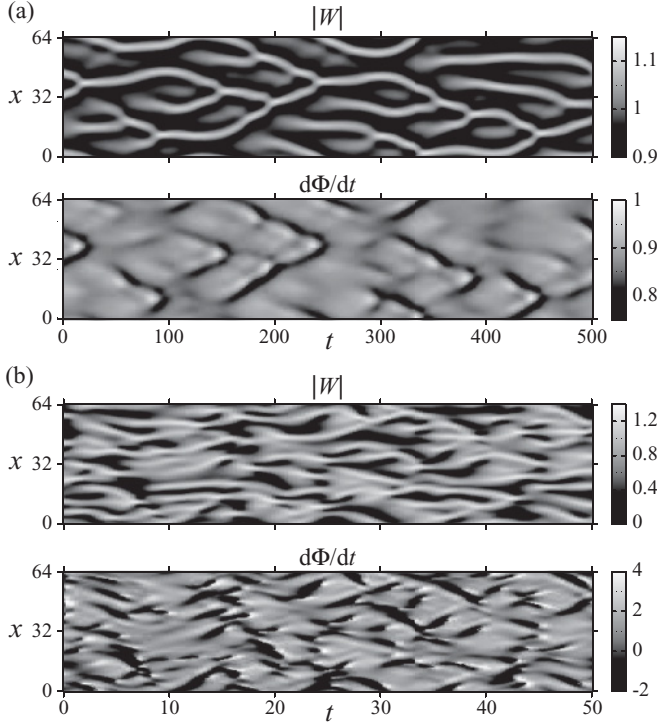


FIG. 8. Spatiotemporal dynamics of the phase turbulence at  $\alpha = 2.0$  and  $\beta = -0.91$  (a) and the amplitude turbulence at  $\alpha = 2.5$  and  $\beta = -2.0$  (b) in the CGL equation with PBC. The system size is  $L = 64$  for both cases. The gray scale covers the whole range of the values taken by  $|W|$  and  $d\Phi/dt$  except for the phase velocity  $d\Phi/dt$  in the amplitude turbulence (b) showing frequent phase slips (bright and dark spots). Notice the different time scales between (a) and (b).

created and annihilated [Fig. 8(b)]. The observed dynamics is chaotic both in amplitude and in phase for the amplitude turbulence, while in the phase turbulence regime, where no phase slips occur, it has usually been considered that only the phase  $\Phi(x, t)$  is active and the amplitude is effectively slaved to it [6]. Below we show, among other things, that this difference between amplitude turbulence and phase turbulence is reflected in the structure of the physical Lyapunov modes, thus rooting it on a firm basis.

### B. Amplitude turbulence

We first focus on the amplitude turbulence regime, in which the amplitude and the phase evolve chaotically on rather short time and length scales. Specifically, we use  $\alpha = 2.5$ ,  $\beta = -2.0$ ,  $L = 64$ , and  $k_{\text{cut}} = 31 \times 2\pi/L$ . Data are recorded over a period of about  $10^7$  after a transient period of  $2.5 \times 10^4$ .

Figure 9 shows the Lyapunov spectrum in the amplitude turbulence regime. A stepwise region is present, as in the KS equation, but here the multiplicity of each step is four and the spatiotemporal evolution of CLVs in the stepwise region exhibits traveling waves (Fig. 10) instead of the stationary wave found in the KS equation [Fig. 2(c)]. Traveling waves are the natural modes here, as can be readily seen from the linear stability analysis of the null solution  $W(x, t) = 0$ , which gives  $\exp[i(\pm kx - \omega t) + \Lambda t]$  with  $\Lambda = 1 - k^2$  and  $\omega = \alpha k^2$ . This makes the modes with the wave number  $k$

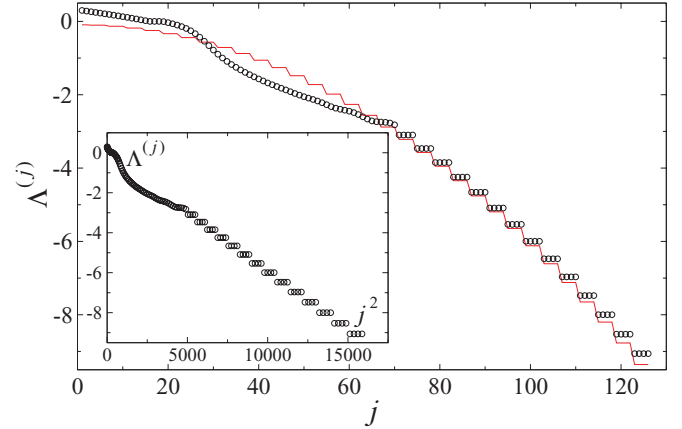


FIG. 9. (Color online) Lyapunov spectrum for the CGL amplitude turbulence. The stepwise structure starts at  $j = 71$ . The red dashed line indicates  $\Lambda^{(j)} = 1 - k^2 - 2\langle |W|^2 \rangle$  derived by Garnier and Wójcik for pure Fourier perturbations [36]. (Inset) The same data against  $j^2$ . The Kaplan-Yorke dimension in this case is about 28.6.

and  $-k$  distinguishable, albeit degenerate, and thus leads to the additional multiplicity of two in the CGL amplitude turbulence. Indeed, each CLV in the stepwise region shows a sharp peak in the power spectrum, located at the trivially determined wave number of the  $j$ th traveling wave, namely, at  $k = [(j + 1)/4]2\pi/L$  (Fig. 11). The values of the Lyapunov exponents therefore decrease as  $\Lambda^{(j)} \approx -k^2 \sim -j^2$  for large  $j$  (inset of Fig. 9). A better estimate was obtained by Garnier and Wójcik [36], who derived  $\Lambda^{(j)} = 1 - k^2 - 2\langle |W|^2 \rangle$  for these stepwise exponents (red dashed line in Fig. 9), assuming perturbations of pure Fourier modes. In passing, the degeneracy of  $k$  and  $-k$  modes implies that these two modes can be, in fact, mixed up in a single vector; their CLVs are either in the pure  $k$  mode, in the pure  $-k$  mode, or patches of the two, changing their states very slowly in time (Fig. 10).

In spite of these differences, the spurious modes in the amplitude turbulence are again hyperbolically isolated from any other modes. Figure 12(a) shows the angle distribution  $\rho_v(\theta)$  for pairs of the neighboring Lyapunov modes. Similarly to the KS equation, the functional form of  $\rho_v(\theta)$  sharply changes at the threshold located at the pair  $(j, j + 1)$  with

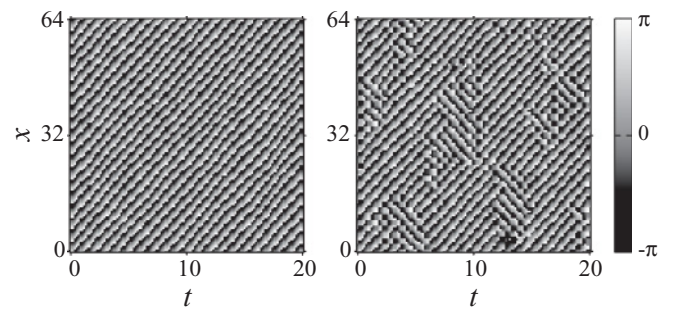


FIG. 10. Spatiotemporal evolution of a typical CLV in the spurious region ( $j = 78$ ) for the CGL amplitude turbulence. The phase component  $\arg \delta W^{(j)}$  is plotted. The two plots are from the same trajectory but at two distant periods of time, showing pure upward traveling waves and patches of upward and downward waves, respectively.

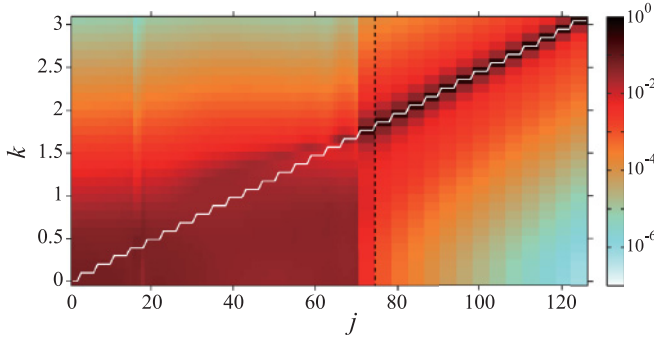


FIG. 11. (Color online) Spatial power spectrum  $S_j(k)$  of the CLVs for the CGL amplitude turbulence, shown as a function of the wave number  $k$  and the Lyapunov index  $j$ . Given that  $S_j(k)$  and  $S_j(-k)$  are statistically equivalent, their average is shown in the figure. The black dashed line separates the physical and spurious regions at  $N_{\text{ph}} = 74$ . The white solid line indicates  $k = [(j + 1)/4]2\pi/L$ .

$j = N_{\text{ph}} = 74$ , above which the distributions are strictly bounded. The tail of the distribution near the threshold exhibits the same critical decay  $\rho_v(\theta) \sim \exp(-\text{const}/\theta)$  within our numerical precision [Fig. 12(b)]. The absence of tangencies is also checked from the distribution of the angle  $\phi$  between the physical and spurious subspaces spanned by the vectors  $1 \leq j \leq N_{\text{ph}}$  and  $N_{\text{ph}} < j$ , respectively [Fig. 12(c)]. The angle distribution  $\rho_s(\phi)$  is indeed bounded away from  $\phi = 0$ . Though the subspace angle  $\phi$  is smaller than the angle  $\theta$  for any pair of CLVs including a spurious mode,  $\rho_s(\phi)$  eventually decays as  $\exp(-\text{const}/\phi)$  for small  $\phi$  [Fig. 12(d)], confirming the absence of any tangencies. The spurious modes are therefore

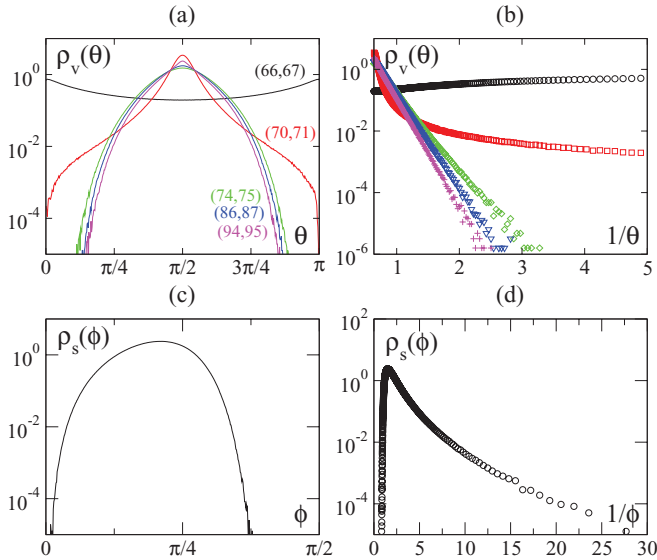


FIG. 12. (Color online) Distributions of the angle between neighboring CLVs (a), (b) and between the physical and spurious subspaces (c), (d) in the CGL amplitude turbulence. (a) Distribution function  $\rho_v(\theta)$  for CLV pairs (66,67), (70,71), (74,75), (86,87), (94,95) from outside to inside. (b)  $\rho_v(\theta)$  versus  $1/\theta$  for the data shown in (a). The ordinate is averaged over both sides of the distribution. (c) Angle distribution  $\rho_s(\phi)$  between the physical subspace spanned by CLVs of indices  $1 \leq j \leq N_{\text{ph}} = 74$  and the spurious one formed by the remaining CLVs. (d) The same data shown against  $1/\phi$ .

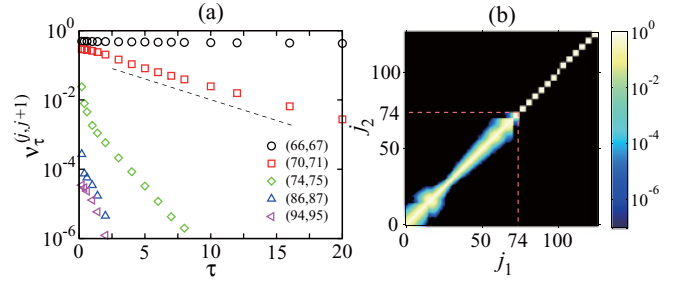


FIG. 13. (Color online) Violation of DOS in the CGL amplitude turbulence. (a) Time fraction  $v_\tau^{(j,j+1)}$  of the DOS violation of the neighbor exponents as a function of  $\tau$ . The dashed line is a guide for the eyes showing an exponential decay. (b)  $v_\tau^{(j_1,j_2)}$  for arbitrary pairs with  $\tau = 16$ . The black color indicates  $v_\tau^{(j_1,j_2)} = 0$ , that is, hyperbolically isolated pairs. The red dashed lines indicate the threshold  $N_{\text{ph}} = 74$  between the physical and spurious modes.

isolated from any other modes outside the step they belong to in the Lyapunov spectrum, and from any linear combination of the physical modes, in the same way as for the KS equation.

Concerning the DOS violation, though the time fraction  $v_\tau^{(j_1,j_2)}$  measured with small  $\tau$  is not zero even in the spurious region, the same threshold  $N_{\text{ph}} = 74$  is found when we consider larger values of  $\tau$  [Fig. 13(a)]. Contrary to what happens for  $j_1, j_2 \leq N_{\text{ph}}$ ,  $v_\tau^{(j_1,j_2)}$  for  $j_2 > N_{\text{ph}}$  decreases faster than exponentially, though exponential decay may persist up to the largest  $\tau$  explorably near the threshold. This decay faster than exponential implies the existence of a finite  $\tau$  beyond which  $v_\tau^{(j_1,j_2)}$  is zero. With such large  $\tau$  values, every quartet of the spurious modes is indeed hyperbolically isolated from all the other modes, while the physical modes including those in the first apparent step are connected to the neighbors [Fig. 13(b)]. All these results are consistent with what we have found for the KS equation and determine exactly the number of the physical modes, here at  $N_{\text{ph}} = 74$ .

### C. Phase turbulence

We now turn our attention to the phase-turbulence regime [Fig. 8(a)], in which the dynamics is believed to be governed by the phase variable [6]. We choose here  $\alpha = 2.0$ ,  $\beta = -0.91$ , and  $L = 96$ . The cutoff wave number is  $k_{\text{cut}} = 31 \times 2\pi/L$  unless otherwise indicated. In this phase-turbulence regime, the global phase difference is conserved because of the absence of phase slips. Here we set it to be zero, in which case phase dynamics is well-described by the KS equation, at least close to the Benjamin-Feir line [6]. Data are recorded over a period of about  $10^6$  after a transient period of  $5 \times 10^4$  is discarded.

In this regime, the Lyapunov spectrum shown in Fig. 14 reveals an interesting structure; now there are much fewer physical modes (black circles) than in the amplitude turbulence and they are followed by three distinct regions of spurious modes. The modes in the first spurious region resemble those in the KS equation (red squares), while in the last part of the spectrum we find a structure similar to that in the CGL amplitude turbulence (blue triangles). In between, the spurious modes appear to be mixed up with the modes that would take part in the physical region in the amplitude turbulence

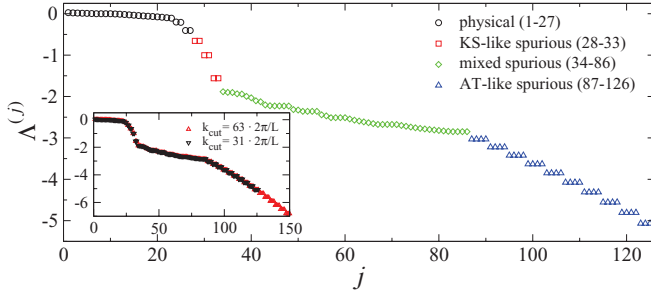


FIG. 14. (Color online) Lyapunov spectrum  $\Lambda^{(j)}$  for the CGL phase turbulence. Different symbols correspond to different regions of the Lyapunov modes (see text). The Kaplan-Yorke dimension in this case is about 14.6. (Inset) Lyapunov spectra with different spatial resolutions.

regime, as suggested from the rather smooth structure of the spectrum (green diamonds). We shall therefore refer to these spurious modes as KS-like, amplitude-turbulence-like (AT-like), and mixed, respectively, as will be justified later. The exact indices for all the thresholds will be given as well from their hyperbolicity properties. Increasing the spatial resolution merely results in adding further AT-like spurious modes at the end of the spectrum without changing the essential features of the existing modes (inset of Fig. 14).

Figure 15 shows the spatial power spectra of the associated CLVs. This justifies the above classification of the spurious modes; in the physical region the power spectrum of the CLVs reflects that of the trajectory (not shown) and thus it hardly changes with varying index, except for those associated with null Lyapunov exponents or too close to the threshold. For the KS-like and AT-like spurious modes, the CLVs are nearly sinusoidal, as indicated by a sharp peak in their power spectrum. Their peak wave number  $k_{\text{peak}}$  is determined by the same trivial geometrical rules as those for the KS equation and for the amplitude turbulence, respectively:  $k_{\text{peak}} = [j/2]2\pi/L$  for the former and  $k_{\text{peak}} = [(j+1)/4]2\pi/L$  for the latter

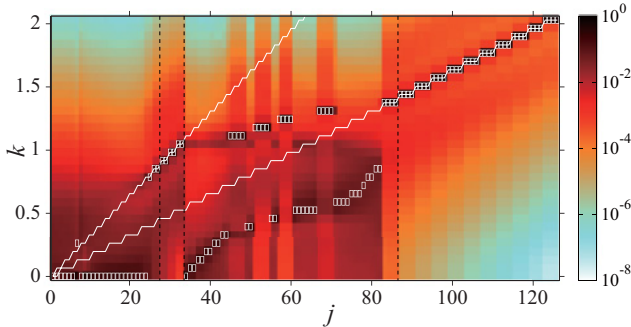


FIG. 15. (Color online) Spatial power spectrum  $S_j(k)$  of the CLVs for the CGL phase turbulence, shown as a function of the wave number  $k$  and the Lyapunov index  $j$ . Given that  $S_j(k)$  and  $S_j(-k)$  are statistically equivalent, their average is shown in the figure. The peak wave number for each  $j$  is indicated by the white rectangles. The black dashed lines separate the four regions of the Lyapunov modes. The white solid lines indicate  $k = [j/2]2\pi/L$  (upper line) and  $k = [(j+1)/4]2\pi/L$  (lower line), which are the trivial peak wave numbers found for the spurious modes in the KS equation and in the CGL amplitude turbulence, respectively.

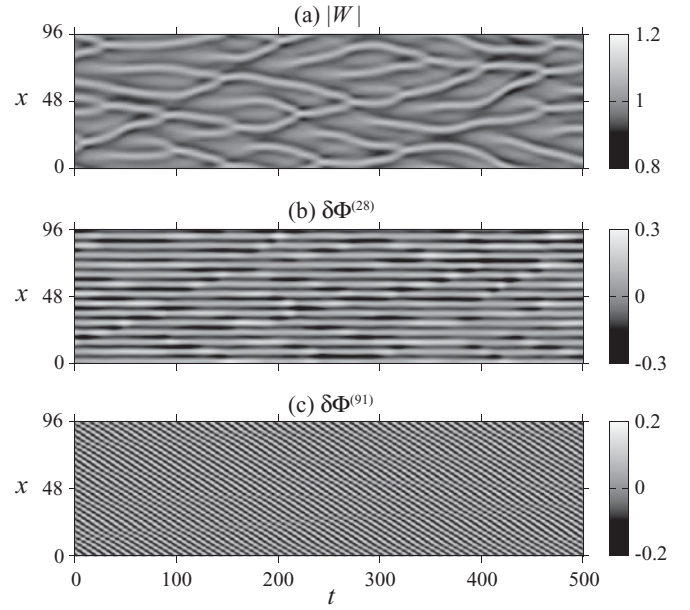


FIG. 16. Spatiotemporal evolution of a typical KS-like and AT-like mode in the CGL phase turbulence. (a) Amplitude  $|W|$  of the dynamics. (b), (c) Phase component  $\delta\Phi^{(j)}$  of the CLV for the KS-like spurious mode at  $j = 28$  (b) and for the AT-like one at  $j = 91$  (c).

(white solid lines in Fig. 15). In contrast, the mixed spurious region consists of two branches; one continues from the KS-like spurious modes, corresponding to the upper branch in the peak wave number, and the other continues from the physical modes, forming the lower branch. The two branches finally merge, marking the start of the AT-like spurious region.

The correspondence of these modes to the spurious modes of the KS equation and the CGL amplitude turbulence is not found only in the peak wave number. Figure 16 displays the spatiotemporal structure of a typical KS-like and AT-like spurious mode, showing specifically the local phase shift  $\delta\Phi^{(j)}$  onto the phase field  $\Phi$  [Eq. (9)] induced by the corresponding CLV. It is defined by the relation

$$\delta W^{(j)} = [\delta A^{(j)} + i(A\delta\Phi^{(j)} + \beta\delta A^{(j)})]e^{i(\Phi + \beta \ln A)}, \quad (10)$$

obtained with  $A(x,t) \equiv |W(x,t)|$  and  $W = Ae^{i(\Phi + \beta \ln A)}$ , and is a natural counterpart of the vector component  $\delta u^{(j)}$  for the KS equation. In this phase shift field, the KS-like spurious modes [Fig. 16(b)] reveal essentially stationary wave structure with amplitude modulated by the dynamics, in the same way as those for the KS equation [Fig. 2(c)]. Similarly, the same traveling wave structure as in the amplitude turbulence regime (bottom insets of Fig. 9) is found for the AT-like spurious modes [Fig. 16(c)].

In spite of this rather complicated internal structure of the spurious region, the essential feature of the spurious modes remains the same; they are all hyperbolically isolated from the physical modes. Figures 17(a)–17(d) shows the angle distributions for pairs of neighboring Lyapunov modes near the thresholds. For the threshold between the physical and KS-like spurious modes, the first two visible doublets in the Lyapunov spectrum ( $24 \leq j \leq 27$ ) belong, in fact, to the physical region [see the pair (25,26) in Figs. 17(a) and 17(b)], whereas the

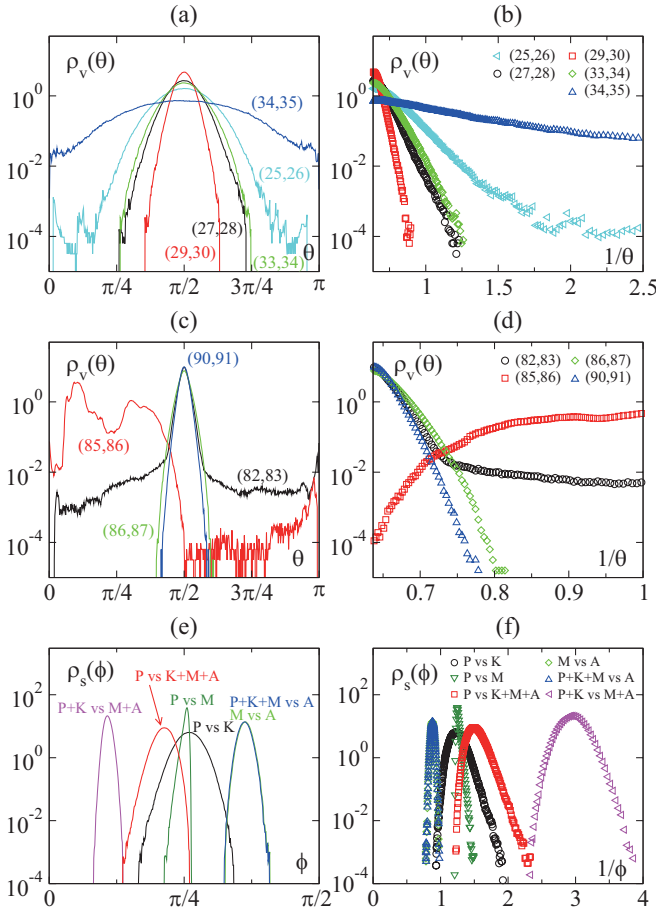


FIG. 17. (Color online) Distributions of the angle between neighboring CLVs (a)–(d) and between pairs of subspaces (e), (f) in the CGL phase turbulence. (a) Distribution function  $\rho_v(\theta)$  for CLV pairs (34,35), (25,26), (33,34), (27,28), (29,30) from outermost to innermost. They determine the thresholds for the physical, KS-like, and mixed regions. (b)  $\rho_v(\theta)$  versus  $1/\theta$  for the data shown in (a). The ordinate is averaged over both sides of the distribution. (c)  $\rho_v(\theta)$  for CLV pairs (82,83), (85,86), (86,87), (90,91) as indicated by the labels. They are relevant to the threshold between the mixed and AT-like regions. (d)  $\rho_v(\theta)$  versus  $1/\theta$  for the data shown in (c). The ordinate is averaged over both sides of the distribution. (e) Subspace angle distributions  $\rho_s(\phi)$ . The abbreviations P, K, M, and A refer to the physical modes ( $1 \leq j \leq 27$ ), the KS-like spurious modes ( $28 \leq j \leq 33$ ), the mixed spurious modes ( $34 \leq j \leq 86$ ), and the AT-like spurious modes ( $87 \leq j \leq 126$ ), respectively. The rightmost two curves overlap almost perfectly. (f) The same data as (e) shown against  $1/\phi$ .

first KS-like spurious mode is found at  $j = 28$  [pair (27,28) in (a) and (b)]. The KS-like spurious modes are hyperbolic with respect to any other modes outside the step including other KS-like doublets [pair (29,30) in (a) and (b)] and the mixed modes [pair (33,34) in (a) and (b)]. In contrast, the mixed spurious modes, despite the absence of tangencies with any physical, KS-like, and AT-like modes, do have tangencies inside the mixed region [pair (34,35) in (a) and (b) and pairs (82,83), (85,86) in (c) and (d)]. The asymmetry (with respect to  $\pi/2$ ) of some of the distributions is due to the finite length of the simulations, indicating that correlations relax very slowly for these pairs of CLVs. In the AT-like spurious region, every

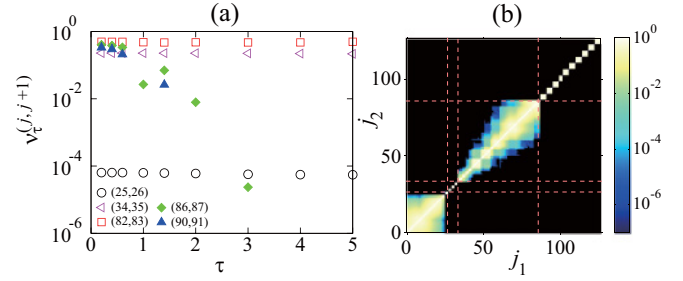


FIG. 18. (Color online) Violation of DOS in the CGL phase turbulence. (a) Time fraction  $\nu_\tau^{(j,j+1)}$  of the DOS violation for pairs of neighboring Lyapunov exponents as a function of  $\tau$ . Pairs with and without tangencies in the angle distributions [Figs. 17(a) and 17(b)] are denoted by open and solid symbols, respectively. All pairs in the KS-like spurious region ( $28 \leq j \leq 33$  excluding those in the same doublet) perfectly satisfy DOS, that is,  $\nu_\tau^{(j_1,j_2)} = 0$ , even with such a small value of  $\tau$  as 0.2. (b)  $\nu_\tau^{(j_1,j_2)}$  for arbitrary pairs with  $\tau = 4$ . The black color indicates  $\nu_\tau^{(j_1,j_2)} = 0$ , that is, hyperbolic isolated pairs. The red dashed lines indicate the thresholds of the four regions.

quartet is again isolated from any other modes including other quartets in the AT-like region [pairs (86,87), (90,91) in (c) and (d)]. From all these observations, we precisely determine the number of the physical modes at  $N_{\text{ph}} = 27$ , as well as the index of all the internal thresholds of the spurious region as illustrated in Fig. 14.

The violation of DOS corroborates this view (Fig. 18). Though the time fraction of the DOS violation  $\nu_\tau^{(j_1,j_2)}$  is found to decrease sometimes not monotonically with respect to  $\tau$  for mixed spurious modes, presumably related to their long-lasting correlation,  $\nu_\tau^{(j_1,j_2)}$  decays faster than exponentially for any pair which lacks tangencies in the angle distributions [Fig. 18(a)]. The matrix representation of  $\nu_\tau^{(j_1,j_2)}$  with a sufficiently large  $\tau$ , which is only  $\tau = 4$  here, clearly shows that all KS-like doublets and AT-like quartets are completely isolated, while the mixed spurious modes are densely connected inside the mixed region but with none of the modes outside [Fig. 18(b)].

Similarly to the cases studied above, not only pairs of single Lyapunov modes, but any linear combination of them is strictly hyperbolic if they are chosen from different regions. This is best demonstrated by the angle distributions for subspaces spanning the four regions [Figs. 17(e) and 17(f)]. Subspaces formed by the Lyapunov modes spanning different regions have always nonzero angles between each other. The angle distribution  $\rho_s(\phi)$  shows the critical decay with essential singularity, that is,  $\rho_s(\phi) \sim \exp(-\text{const}/\phi)$ , or decays even faster [Fig. 17(f)]. In particular, all the spurious modes, including mixed ones, do not have any tangency with any of the physical modes and their Lyapunov exponents are always negative. The two essential properties of the spurious modes are thus satisfied by all of them. This implies that they exponentially decay to zero without interacting with any physical modes, though some spurious modes are internally entangled, and thus they are not expected to affect the dynamics in the global attractor.

These results for the amplitude turbulence and the phase turbulence lead us to interpret that amplitude degrees of freedom are slaved in the phase turbulence regime, and this

produces the mixed spurious region in place, being mixed with the KS-like spurious modes. To test this speculation, we compare the structure of the CLVs with that expected under the assumption of the amplitude slaved by the phase. The dynamics in the phase turbulence regime indicates that the amplitude  $A(x,t) \equiv |W(x,t)|$  is almost uniquely determined by the local phase curvature  $\Psi(x,t) \equiv \partial^2 \Phi / \partial x^2$ , that is,

$$A(x,t) \approx A(\Psi(x,t)), \quad (11)$$

as shown in Fig. 19(a). This then implies the following amplitude-phase relation for the CLVs, as long as they result from the slaved amplitude:

$$\delta A_p^{(j)}(x,t) \approx \frac{\partial A}{\partial \Psi} \delta \Psi^{(j)}(x,t), \quad (12)$$

where  $\delta A$  and  $\delta \Psi$  are the vector components corresponding to  $A$  and  $\Psi$ , obtained through Eq. (10) and  $\delta \Psi^{(j)} = \partial^2 \delta \Phi^{(j)} / \partial x^2$ , and the subscript p denotes the estimate under the assumption (11). Comparing  $\delta A_p^{(j)}$  with the actual amplitude component

$\delta A^{(j)}$ , one can examine to what extent the assumption of the slaved amplitude holds for each Lyapunov mode.

The result is shown in Figs. 19(b)–19(f), which displays the density plots of  $\delta A_p^{(j)}$  versus  $\delta A^{(j)}$  for a typical CLV in each region of the Lyapunov spectrum. For the CLVs in the physical region [Fig. 19(b)] the prediction of Eq. (12) holds as accurately as the slaved amplitude assumption (11) does for the dynamics [Fig. 19(a)]. It is also the case, albeit with somewhat larger deviations, for the KS-like spurious modes [Fig. 19(c)]. This is quite natural because the physical modes should reflect the dynamics, which is governed by the phase here, and the KS-like spurious modes are present in the KS equation, which phenomenologically describes such phase instability. On the other hand, the mixed spurious modes, which comprise degrees of freedom not obeying the slaved amplitude assumption, exhibit very different structures. For those which belong to the lower branch in the peak wave number spectrum [Fig. 19(d)], the amplitude  $\delta A$  varies widely, while the phase component stays essentially quiescent, so does  $\delta A_p$ . This implies that these modes comprise mostly the amplitude degrees of freedom, which underpins the view that independent amplitude degrees of freedom are lost and become spurious in this phase turbulence regime. In contrast, the mixed spurious modes in the upper branch are still influenced by Eq. (12) [Fig. 19(e)]. This indicates that these modes essentially originate from the KS-like modes, but the slaved amplitude assumption holds only very loosely, probably because of the mixture with the spurious amplitude degrees of freedom in the lower branch. Finally, for the AT-like spurious modes the slaved amplitude assumption does not work any more [Fig. 19(f)]. The two amplitudes rather rotate in the  $\delta A$ - $\delta A_p$  plane irrespective of the dynamics, which is in line with their trivial traveling wave structure [Fig. 16(c)].

In summary, we have found that in the phase turbulence regime the tangent-space dynamics consists of the physical modes and the three sets of spurious modes, all of which are hyperbolically decoupled from any physical mode. These physical modes essentially stem from the phase degrees of freedom of the CGL equation, unlike in the amplitude turbulence where both phase and amplitude participate in the physical modes. The loss of the amplitude degrees of freedom considerably reduces the number of the physical modes and produces instead the mixed spurious modes. This view is supported by the fact that the mixed spurious region starts at the exponent value close to  $-2$  [Fig. 14(a)], which is the stability of the amplitude of a single Ginzburg-Landau oscillator. Our results, therefore, corroborate the qualitative picture of the phase turbulence that the dynamics is governed by the phase, whereas, practically, the amplitude modes do not serve as independent degrees of freedom as they are essentially slaved by the phase. It should be noted, however, that the physical and spurious modes do *not* correspond exactly to the phase and amplitude degrees of freedom, respectively, as can be seen from the weak violation of Eqs. (11) and (12) in the dynamics and the physical modes [Figs. 19(a) and 19(b)]. This implies that the phase reduction is not exact in the phase turbulence, in line with results from past studies [37]. To extract a proper set of global variables describing the dynamics is a difficult problem, which will be briefly discussed in Sec. VI.

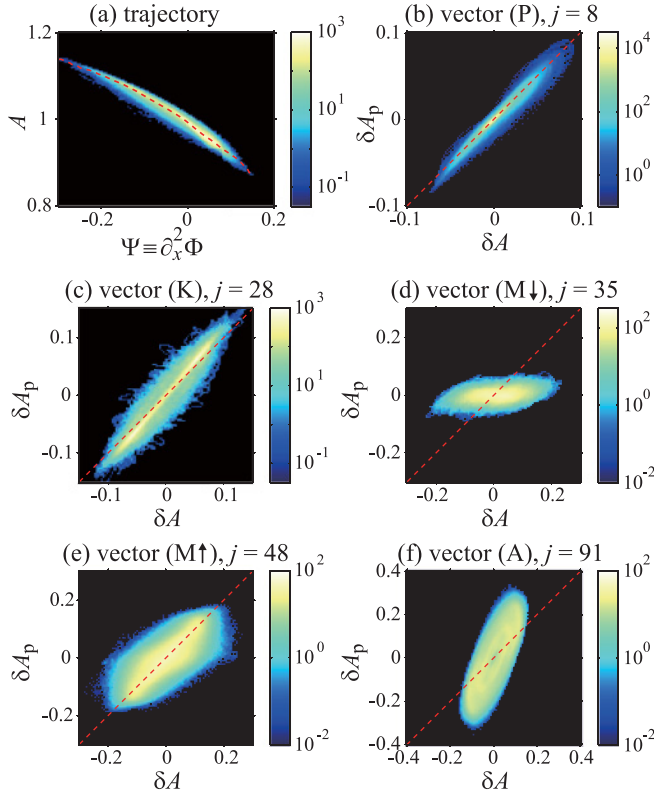


FIG. 19. (Color online) Density plots showing the structure of the trajectory (a) and of the CLVs (b)–(f) in the CGL phase turbulence. (a) Density plot for the amplitude  $A$  and the phase curvature  $\Psi$  of the trajectory. The red dashed curve indicates the averaged value of  $A$  for each bin of  $\Psi$ . (b)–(f) Density plots for the CLVs, comparing the actual amplitude component  $\delta A$  with that expected from the assumption of the slaved amplitude,  $\delta A_p$  [Eq. (12)]. The red dashed lines indicate  $\delta A_p = \delta A$ . The abbreviations P, K, M, and A denote a physical, KS-like, mixed, and AT-like mode, respectively. The upward and downward arrows next to M denote the upper and lower branches, respectively, in the plot of the peak wave number [Fig. 14(b)]. All the data shown here are recorded during two periods of length  $10^3$  separated by an interval of roughly  $10^6$ .

#### IV. 1D LATTICE SYSTEMS

So far we have studied two generic dissipative PDEs and found the separation of a finite number of physical modes from the remaining spurious modes. We have argued that the physical modes correspond to the active degrees of freedom necessary to describe the dynamics and that they probably provide the tangent-space representation of the inertial manifold. Although the concept of the inertial manifold is of great importance in such PDE systems, the existence of such a smooth invariant manifold of dimension smaller than the phase space is not restricted to PDEs. We therefore study spatially discrete systems in this section, one defined with discrete time (i.e., map) and another with continuous time (i.e., ordinary differential equation).

##### A. 1D lattice of coupled tent maps

First we consider the following 1D lattice of diffusively coupled tent maps:

$$\begin{aligned} x_i^{t+1} &= f(x_i^t) + \frac{K}{2} [f(x_{i+1}^t) - 2f(x_i^t) + f(x_{i-1}^t)] \\ &= \left[ 1 + \frac{K}{2} \mathcal{D} \right] f(x_i^t), \end{aligned} \quad (13)$$

with  $i = 1, 2, \dots, L$ ,  $f(x) = 1 - \mu|x|$ , and the discrete Laplacian operator

$$\mathcal{D}f(x_i^t) \equiv f(x_{i+1}^t) - 2f(x_i^t) + f(x_{i-1}^t). \quad (14)$$

In such systems, obviously, varying the spatial resolution does not make sense. Instead, we increase the coupling constant  $K$  so that local dynamical variables  $x_i^t$  possess stronger correlations with their neighbors, possibly reducing the number of effective degrees of freedom.

Here we use  $\mu = 1.1$ ,  $L = 256$ , and PBC. With this value of  $\mu$ , the local map exhibits four-band chaos. We start from random initial conditions distributed only within one of the bands, and hence the coupled-map lattice shows period-4 collective behavior. Data are recorded over roughly  $5 \times 10^5$  time steps after a transient of nearly the same length.

Figure 20 shows the Lyapunov spectra of this coupled-map lattice for two values of the coupling constant  $K$ . As expected, while for moderate strengths of the coupling the Lyapunov spectrum does not show any splitting of the structure (e.g., red squares in Fig. 20), strengthening the coupling induces a stepwise structure at the end of the Lyapunov spectrum [ $K = 0.65$  in Fig. 20 (black circles)], similarly to what happens in PDEs.

Concerning the structure of the CLVs, the Lyapunov modes in the smooth region, particularly at the beginning of the spectrum, tend to be localized at one of the antinodes (or a few of them) of the wavy structure of the dynamics [Figs. 21(a) and 21(b)]. Over long time scales the weight shifts from an antinode to another (or from some to others). In contrast, those in the stepwise region exhibit stationary wave structures [Fig. 21(c)] similar to the spurious modes in the KS equation [Fig. 2(c)].

A difference from the PDE systems is found, however, in the way the peak wave number of the spurious modes is determined. Figure 22 shows the spatial power spectra

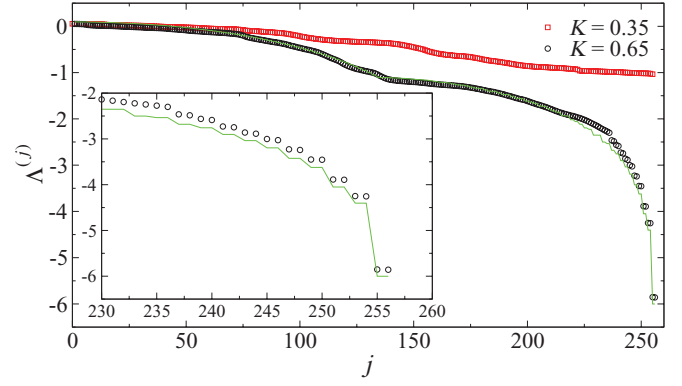


FIG. 20. (Color online) Lyapunov spectrum for the coupled tent maps (13) with varying coupling constant  $K$ . (Inset) Close-up of the end of the spectrum for  $K = 0.65$ . The green lines show the spectrum estimated under the Fourier mode approximation (see text). The Kaplan-Yorke dimension for  $K = 0.65$  is about 39.9.

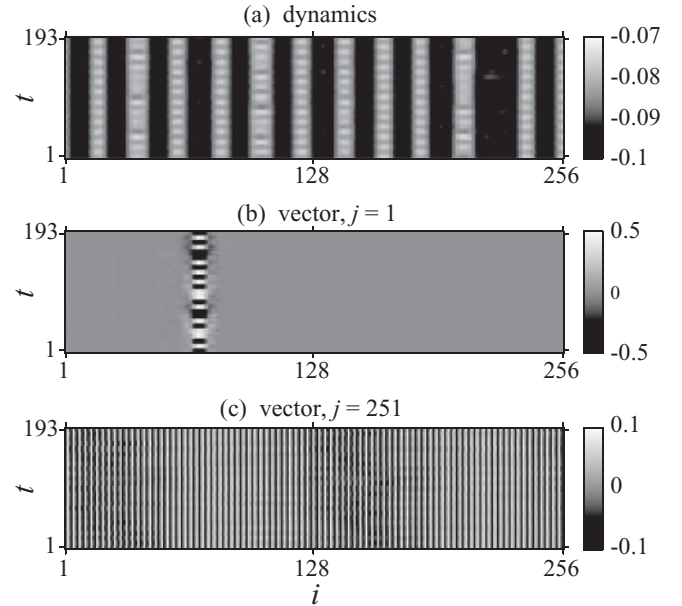


FIG. 21. Spatiotemporal evolution of the dynamics  $x_i^t$  (a), of a physical Lyapunov mode at  $j = 1$  (b), and of a spurious Lyapunov mode at  $j = 251$  (c) in the coupled tent maps with  $K = 0.65$ . The spatial profiles are plotted every eight time steps in order to capture the internal structure of the period-4 collective behavior.

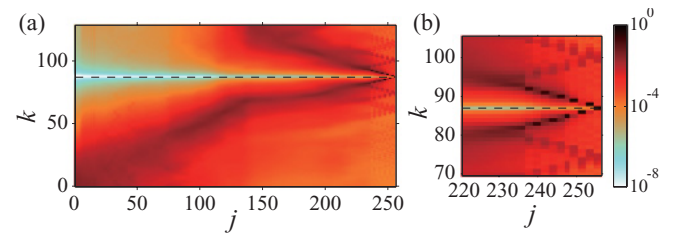


FIG. 22. (Color online) Spatial power spectrum of the CLVs for the tent coupled-map lattice with  $K = 0.65$ , shown as a function of the (integer) wave number  $k$  and the Lyapunov index  $j$ . The dashed line indicates  $k = 87$ , which gives the smallest eigenvalue for the coupling operator  $1 + (K/2)\mathcal{D}$  (see text). The panel (b) is a close-up of (a) near the peak wave numbers of the CLVs at the end of the Lyapunov spectrum.

of the CLVs. While in PDEs the peak wave number in the stepwise region increases monotonously according to trivial geometrical rules (Figs. 3 and 15, except for the special case of the mixed spurious modes in the CGL phase turbulence), in the coupled-map lattice it forms two branches, one increasing and the other decreasing, which eventually join at  $j = L$  at a certain wave number [dark red spots in Fig. 22(b)]. In fact, this is again a simple consequence of the nearly sinusoidal structure of the CLVs in the stepwise region. The Fourier modes  $\delta W_i = \sin(2\pi ik/L)$  and  $\cos(2\pi ik/L)$  with integer  $k$  are eigenvectors of the coupling operator  $1 + (K/2)\mathcal{D}$  in Eq. (13). Their associated eigenvalue is  $1 - K[1 - \cos(2\pi k/L)]$ , whose contribution to the Lyapunov exponent is  $\log |1 - K[1 - \cos(2\pi k/L)]|$ . Since it is not a monotonous function of  $k$ , the peak wave number in the power spectra, too, is not monotonous. For  $K = 0.65$ ,  $k = 87$  gives the eigenvalue closest to zero, and therefore is the peak wave number for the CLV of the smallest Lyapunov exponent

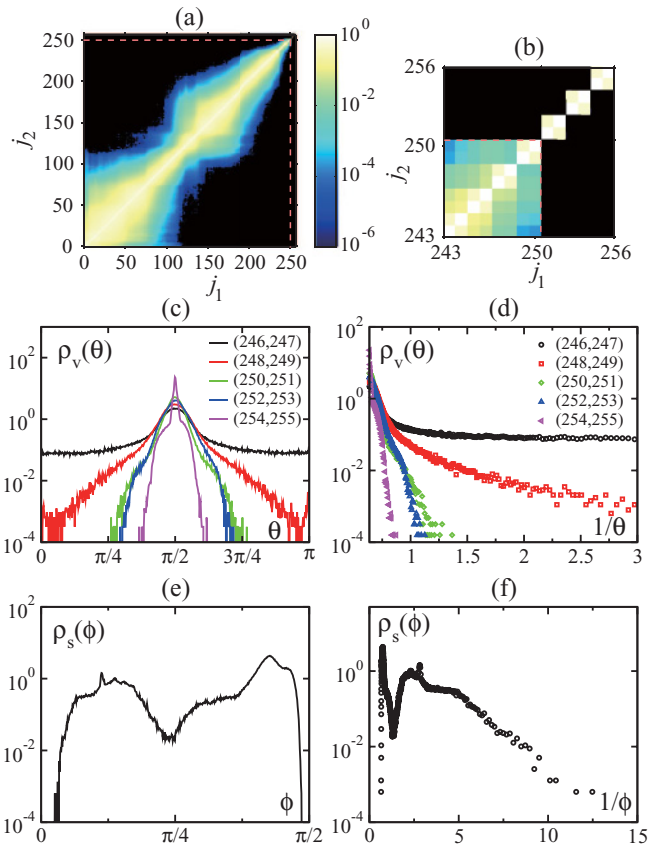


FIG. 23. (Color online) Hyperbolicity properties for the tent coupled-map lattice with  $K = 0.65$ . (a) Time fraction  $v_\tau^{(j_1, j_2)}$  of the DOS violation for arbitrary pairs with  $\tau = 2$ . The black color indicates  $v_\tau^{(j_1, j_2)} = 0$ , that is, hyperbolically isolated pairs. The red dashed lines indicate the threshold  $N_{\text{ph}} = 250$  between the physical and spurious modes. (b) Close-up of (a) near the end of the spectrum. (c) Angle distributions  $\rho_v(\theta)$  for neighboring CLVs of indices (246,247), (248,249), . . . , (254,255) from upper left to lower right. (d)  $\rho_v(\theta)$  against  $1/\theta$ . The ordinate is averaged over both sides of the distribution. (e) Angle distribution  $\rho_s(\phi)$  between the physical subspace ( $1 \leq j \leq 250$ ) and the spurious one ( $251 \leq j \leq 256$ ). (f)  $\rho_s(\phi)$  against  $1/\phi$ .

(dashed line in Fig. 22). Moreover, approximating the contribution from the local map  $f(x)$  to the Lyapunov exponent by  $\log \mu$ , we obtain  $\Lambda = \log |1 - K[1 - \cos(2\pi k/L)]| + \log \mu$ , which indeed captures the qualitative structure of the observed Lyapunov spectrum (Fig. 20).

Despite this apparent difference from PDEs, we identify the same tangent-space decoupling into the physical and spurious modes in this coupled-map lattice. Measuring the time fraction  $v_\tau^{(j_1, j_2)}$  of the DOS violation, we find that the last three doublets of Lyapunov modes are hyperbolically isolated from all the other modes [Figs. 23(a) and 23(b)]. The splitting into the physical and spurious modes can also be confirmed from the angle distributions between CLVs [Figs. 23(c) and 23(d)], as well as that between the physical and spurious subspaces defined by the corresponding CLVs [Figs. 23(e) and 23(f)]. If the manifold of the physical modes is a local approximation of the inertial manifold as we speculate, our results imply that dissipative coupled map lattices may also have an inertial manifold, whose dimension is lower than that of the phase space.

### B. 1D lattice of Ginzburg-Landau oscillators

Now we study another example of the spatially discrete dynamical systems, here defined with continuous time. Specifically, we take the system studied recently by Kuptsov and Parlitz [38], namely a 1D lattice of CGL oscillators,

$$\frac{\partial W_i}{\partial t} = W_i - (1 + i\beta)|W_i|^2 W_i + (1 + i\alpha) \frac{\mathcal{D}W_i}{h^2}, \quad (15)$$

with complex variables  $W_i(t)$  and  $i = 1, 2, \dots, L$ . This can be regarded as a spatial discretization of the CGL equation (8), where the parameter  $h$  denotes the lattice constant and thus behaves similarly unless  $h$  is too large. For small  $h$ , the system is a good approximation of the CGL equation, and hence the decoupling of the physical and spurious modes takes place in the same manner as we have studied in Sec. III. Increasing  $h$ , besides degrading the correspondence to the CGL equation, amounts to increasing the chain length  $hL$  and thus leads to an increase in the number of physical modes. Moreover, Kuptsov and Parlitz [38] reported that, as the number of physical modes increases with  $h$  at the positive end of the Lyapunov spectrum, another set of modes appears at the negative end, which are hyperbolically connected within themselves and whose number also increases with  $h$ . Isolated steps of the spurious modes being replaced from both ends, the authors argued that the two groups finally meet each other and the strict hyperbolic decoupling between them is lost for large  $h$ . However, their claim is based solely on the observation of the structure of the CLVs and the time fraction of the DOS violation with a fixed  $\tau$  [38,39], which cannot fully determine hyperbolic decoupling. Therefore, here we revisit this problem, performing a complete analysis to clarify the nature of the hyperbolic decoupling in this system, and explain this rather peculiar behavior reported by Kuptsov and Parlitz.

In the following, we take the same parameter values as Kuptsov and Parlitz [38], namely,  $\alpha = -2.0$  and  $\beta = 3.0$ , which correspond to the amplitude turbulence regime (cf. Sec. III B), and vary the value of  $h$ . We fix the system size at  $L = 32$  and adopt PBC,  $W_{i+L} = W_i$ . Kuptsov and

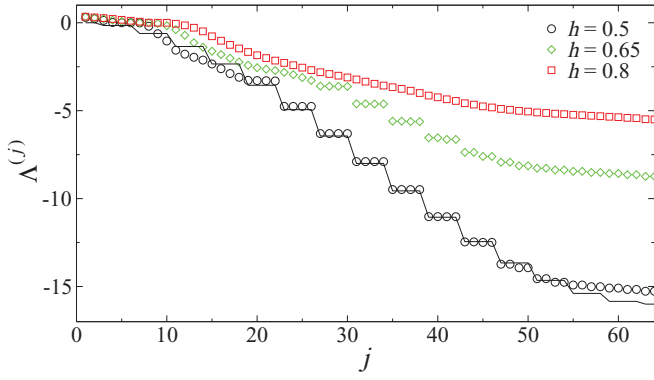


FIG. 24. (Color online) Lyapunov spectrum for the CGL lattice (15) with varying  $h$ . The numerically obtained spectra are shown by the symbols, while the black line indicates the spectrum of the contribution from the coupling term under the Fourier mode approximation for  $h = 0.5$  (see text). The Kaplan-Yorke dimension is about 8.8, 11.6, and 14.7 for  $h = 0.5$ ,  $h = 0.65$ , and  $h = 0.8$ , respectively.

Parlitz used instead a no-flux boundary condition in Ref. [38], but this difference in the boundary conditions intervenes practically only in the multiplicity of the stepwise structure of the Lyapunov spectrum, as we have seen in Sec. II. Time integration is performed with the fourth-order Runge-Kutta method and time step 0.01, over a period of about  $2 \times 10^5$  after a transient of  $2.5 \times 10^4$  is discarded.

Figure 24 shows the Lyapunov spectra of the CGL lattice for varying  $h$ . As reported in Ref. [38], for small  $h$  the spectrum exhibits the stepwise structure (black circles), but it arises in the middle of the spectrum, as opposed to the CGL equation for which the steps continue up to the end of the spectrum. In the CGL lattice, they are instead sandwiched by two smooth regions. With increasing  $h$ , both of these smooth regions grow (green diamonds in Fig. 24) and finally merge (red squares), replacing all the steps in the spectrum. The power spectra of the CLVs in Fig. 25 show that the steps here are again due to the sinusoidal structure of the CLVs, as evidenced by the sharp

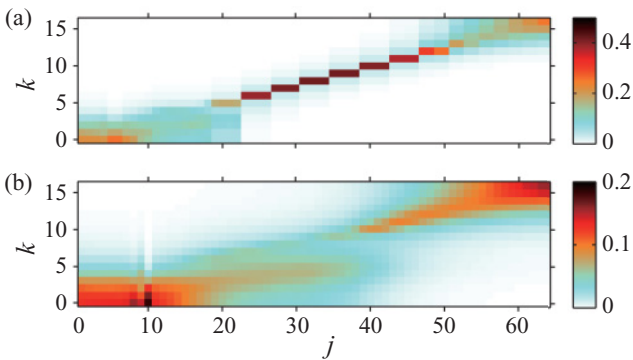


FIG. 25. (Color online) Spatial power spectrum  $S_j(k)$  of the CLVs for the CGL lattice with  $h = 0.5$  (a) and  $h = 0.8$  (b), shown as a function of the (integer) wave number  $k$  and the Lyapunov index  $j$ . Given that  $S_j(k)$  and  $S_j(-k)$  are statistically equivalent, their average is shown in the figure. Note that the color plots are in different linear scales for the sake of clarity.

peaks for the stepwise modes in Fig. 25(a), while CLVs in the two smooth regions do not have obvious wavy structure.

Analyzing hyperbolicity properties of this system reveals that, for small  $h$ , the Lyapunov spectrum splits into three regions, basically according to its stepwise structure (Fig. 26). The first gap in the stepwise region already exhibits clear hyperbolic decoupling of the two modes at the edge, namely, those of indices 22 and 23; for them the CLV angle distribution  $\rho_v(\theta)$  is bounded with a decay faster than  $\exp(-\text{const}/\theta)$  in the tail [black, innermost line and symbols in Figs. 26(a) and

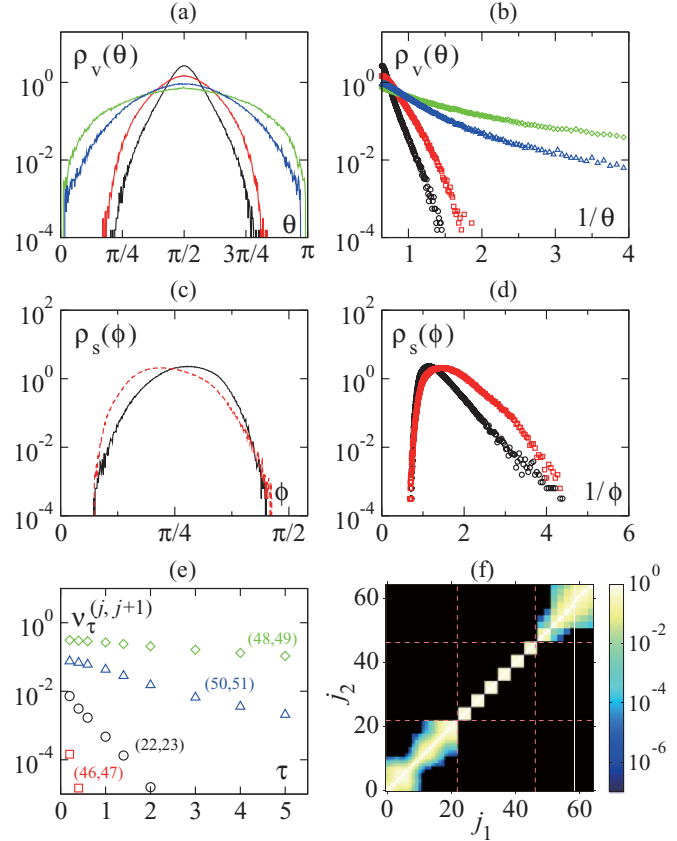


FIG. 26. (Color online) Hyperbolicity properties for the CGL lattice with  $h = 0.5$ . (a) Angle distributions  $\rho_v(\theta)$  for neighboring CLVs of indices (22,23), (46,47), (50,51), and (48,49) from innermost to outermost curve. (b)  $\rho_v(\theta)$  against  $1/\theta$ . The ordinate is averaged over both sides of the distribution. The order of the curves is the same as in (a) from lower left to upper right. (c) Angle distribution  $\rho_s(\phi)$  between the physical subspace ( $1 \leq j \leq N_{\text{ph}}$ ) and the spurious one ( $N_{\text{ph}} + 1 \leq j$ ) with  $N_{\text{ph}} = 22$  (black solid line). The red dashed line shows the angle distribution between the subspaces of indices  $1 \leq j \leq 46$  and  $47 \leq j \leq 64$ , showing the hyperbolic isolation of the tangled spurious subspace. (d) The same plots as (c) but shown against  $1/\phi$  (black circles for the physical and spurious subspaces, and red squares for the other). (e) Time fraction  $v_\tau^{(j,j+1)}$  of the DOS violation for pairs of neighboring Lyapunov exponents as a function of  $\tau$ . (f) Time fraction  $v_\tau^{(j_1,j_2)}$  of the DOS violation for arbitrary pairs with  $\tau = 3$ . The black color indicates  $v_\tau^{(j_1,j_2)} = 0$ , that is, hyperbolicity isolated pairs. The red dashed lines indicate the threshold  $N_{\text{ph}} = 22$  between the physical and spurious modes and that between the stepwise spurious modes  $1 \leq j \leq 46$  and the tangled spurious modes  $47 \leq j \leq 64$ .

26(b)], and the time fraction of the DOS violation  $\nu_\tau^{(22,23)}$  decreases faster than exponentially [black circles in Fig. 26(e)]. This fixes the number of physical modes at  $N_{\text{ph}} = 22$ . The decoupling holds similarly for any pair of CLVs sandwiching this threshold [Fig. 26(f)], as well as between the physical and spurious subspaces, defined at this index [black solid line and circles in Figs. 26(c) and 26(d)].

The spurious subspace in this system, however, consists of the central stepwise region and the smooth region at the end of the Lyapunov spectrum (Fig. 24). In the former, quartets of Lyapunov modes are isolated from all the other modes [Fig. 26(f)] as is usually the case for the spurious modes, while in the latter, specifically here for indices larger than 46, the spurious modes are internally connected [Figs. 26(a), 26(b), 26(e), and 26(f)] in a way similar to the mixed spurious modes in the CGL phase turbulence [see, e.g., Fig. 18(b)]. These are the modes found by Kuptsov and Parlitz [38], though in their work there remained ambiguity in the hyperbolicity properties as discussed above. Here we confirm that these modes are indeed connected internally, but never with any physical or stepwise spurious mode, both from the DOS assay with varying  $\tau$  and from the CLV angle distribution [Figs. 26(a), 26(b), 26(e)]. For this property, we call these modes tangled spurious modes. The subspace composed of them is also hyperbolically isolated from its complementary [red dashed line and squares in Figs. 18(c) and 18(d)]. One should be reminded that the difference between the tangled spurious modes and the physical ones lies in the sign of their Lyapunov exponents; while the exponents for the physical modes can take any sign, those for the spurious modes are always negative, and thus they decay without intervening in the dynamics even if they are internally connected. The effective dimension of the system is therefore always given by the number of the physical modes,  $N_{\text{ph}}$ , without contribution from the tangled spurious modes.

The appearance of the tangled spurious modes is, in fact, again, due to the discrete Laplacian operator of the coupling term in Eq. (15), but it takes place in a different manner as the tent coupled-map lattice because of the continuous time. Here, if we take into account only the coupling term, its growth rate is simply given by the real part of its eigenvalues, specifically  $\Lambda = -(2/h^2)[1 - \cos(2\pi k/L)]$  for the eigenmodes  $e^{2\pi i k i/L}$ . It is monotonic with respect to  $|k|$ , since  $|k|$  varies only up to  $L/2$ , and hence so is the peak wave number of the CLV power spectra in the stepwise region of the Lyapunov spectrum (Fig. 25, to be compared with Fig. 22). The values of the Lyapunov exponent in this region are well approximated by  $\Lambda$  given above with the corresponding  $k$  (black line in Fig. 24). By contrast, for larger  $k$  or  $j$ , the gap in  $\Lambda$  between different  $k$  shrinks, as opposed to the case of the continuous Laplacian operator. This facilitates the order exchange of the Lyapunov exponents, that is, the violation of the DOS, due to their intrinsic fluctuations from the dynamics, and thus produces the tangled spurious modes.

With increasing  $h$ , both physical and tangled spurious modes increase their numbers, replacing the steps of the spurious modes in between (cf., Fig. 24). This finally gives rise to the coalescence of the two groups; as soon as the last physical mode and the first tangled spurious one encounter, all the modes are connected and thus become physical modes.

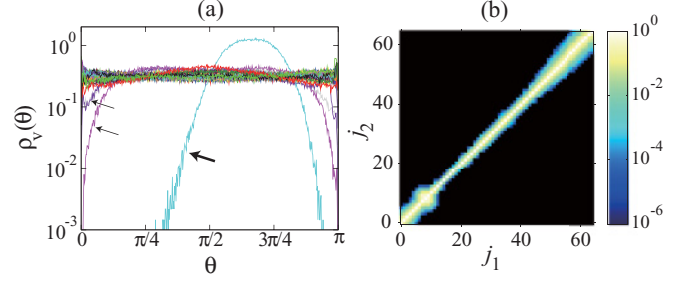


FIG. 27. (Color online) Hyperbolicity properties for the CGL lattice with  $h = 0.8$ . (a) Angle distributions  $\rho_v(\theta)$  for all pairs of neighboring CLVs. Indicated by the arrows are the distributions for the pairs including either or both of the two Lyapunov modes with  $\Lambda^{(j)} = 0$ . All the distributions except the one for the two zero Lyapunov modes, shown by the bold arrow, have finite densities at  $\theta = 0$  and  $\pi$ . (b) Time fraction  $\nu_\tau^{(j_1, j_2)}$  of the DOS violation for arbitrary pairs with  $\tau = 5$ . The black color indicates  $\nu_\tau^{(j_1, j_2)} = 0$ , that is, hyperbolically isolated pairs.

The case for  $h = 0.8$  is shown in Fig. 27. All the CLV angle distributions have finite densities at  $\theta = 0$  and  $\pi$  except for those concerning one or both of the two zero Lyapunov modes [Fig. 27(a)]. The overall connection of the Lyapunov modes is also confirmed from the violation of the DOS [Fig. 27(b)]. That is to say, with increasing  $h$ , the number of the physical modes, or the inertial manifold dimension as we conjecture, is suddenly doubled when the tangled spurious modes join the physical manifold. Although such a large value of  $h$  (around 0.7 in this case) corresponds to a somewhat unphysical situation when we view the CGL lattice as an approximation to the original CGL equation, the physical implication and consequence of this “crisis” remain to be clarified.

## V. 2D KURAMOTO-SIVASHINSKY EQUATION

### A. Definition and numerical scheme

In the previous sections we have investigated the physical-spurious decoupling in 1D dissipative systems. Given the generality of our finding, and also the general existence of a finite-dimensional inertial manifold in dissipative systems, one expects that the same decoupling should also take place in systems of higher dimensions. This is indeed the case, as we shall demonstrate in this section for the 2D KS equation as a generic example.

The 2D KS equation is defined for a real-valued field  $u(x, y, t)$  as [40]

$$\frac{\partial u}{\partial t} = -\nabla^2 u - (\nabla^2)^2 u - \frac{1}{2}(\nabla u)^2, \quad (16)$$

with  $\nabla \equiv (\partial/\partial x, \partial/\partial y)$ ,  $x \in [0, L_x]$ , and  $y \in [0, L_y]$ . Here we adopt PBC  $u(x, y, t) = u(x + L_x, y, t) = u(x, y + L_y, t)$  with  $L \equiv L_x = L_y = 24$  for the sake of simplicity. For integration we use the same operator-splitting method as for the 1D KS equation, with time step 0.005, and the pseudospectral method, with  $k_{\text{cut}} = 10 \times 2\pi/L$ , that is, with  $11 \times 11$  Fourier modes. Integration is performed over a period of roughly  $2 \times 10^5$  after discarding a transient period of 1200.

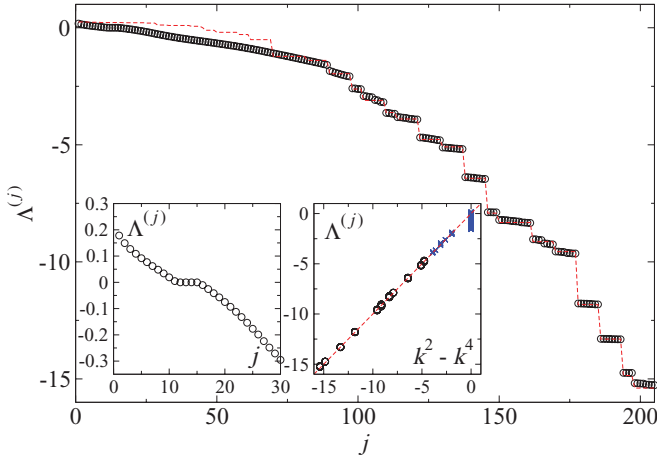


FIG. 28. (Color online) Lyapunov spectrum for the 2D KS equation. The red dashed line shows the values of  $\Lambda^{(j)}$  estimated from the dominating wave number  $(k_x, k_y)$  assigned trivially by the index (see text). (Left inset) Close-up of the beginning of the spectrum. (Right inset) Lyapunov exponent  $\Lambda^{(j)}$  vs  $k^2 - k^4$ , where  $k^2 \equiv k_x^2 + k_y^2$  is the square of the peak wave number for the power spectrum of the  $j$ th CLV (see Fig. 29). Blue crosses and black circles correspond to the physical and spurious modes, respectively. The red dashed line indicates  $\Lambda^{(j)} = k^2 - k^4$ . The Kaplan-Yorke dimension in this case is about 25.1.

### B. Results

For  $L = 24$  the 2D KS equation shows spatiotemporal chaos as in the 1D counterpart studied in Sec. II. This leads to a similar structure of the smooth region of the Lyapunov spectrum [left inset of Fig. 28; cf. Fig. 1(b)], which consists of physical Lyapunov modes carrying information on the dynamics. As for the spurious region, despite its apparently intricate structure in contrast with the 1D spectrum [compare Fig. 28 with Fig. 1(a)], we find that the modes therein possess essentially the same trivial properties, as shown below.

First, unlike the physical modes which show relatively broad power spectra similar to the dynamics [Figs. 29(a)–29(d)], each spurious mode has a spectrum  $S(k_x, k_y)$  sharply peaked around a certain wave number  $k \equiv \sqrt{k_x^2 + k_y^2}$  [Figs. 29(e)–29(f)], which is large and increases with the index. The value of its Lyapunov exponent  $\Lambda^{(j)}$  is then essentially

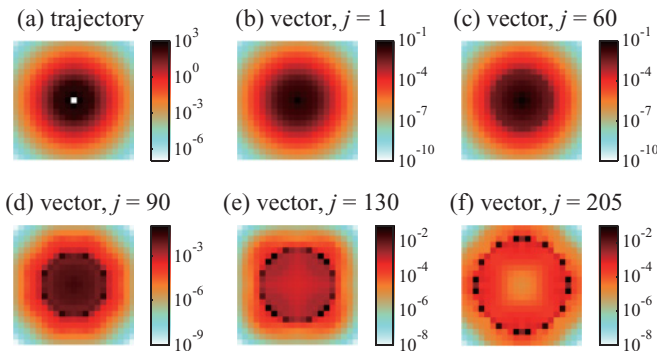


FIG. 29. (Color online) Power spectrum  $S(k_x, k_y)$  of the trajectory (a) and of the CLVs (b)–(f) for the 2D KS equation. The spectra are shown for  $k_x, k_y \in [-k_{\text{cut}}, k_{\text{cut}}]$  with  $k_{\text{cut}} = 10 \times 2\pi/L$ .

determined by the linear terms of the 2D KS equation (16), specifically,  $\Lambda^{(j)} = k^2 - k^4$ , as indeed confirmed in the right inset of Fig. 28 (black circles). Moreover, as in the 1D KS equation, the peak wave numbers  $(k_x, k_y)$  of the spurious modes are trivially determined by the geometry: For a finite box of size  $L_x \times L_y$ , the wave numbers can take values  $k_x = 2\pi n_x/L_x$  and  $k_y = 2\pi n_y/L_y$  with integers  $n_x$  and  $n_y$ . Their values are then assigned to each mode in such a way that the resulting Lyapunov exponent  $\Lambda^{(j)} = k^2 - k^4$  decreases monotonically. Taking into account the multiplicity for 2D PBC, this trivial assignment yields a spectrum indicated by the red dashed line

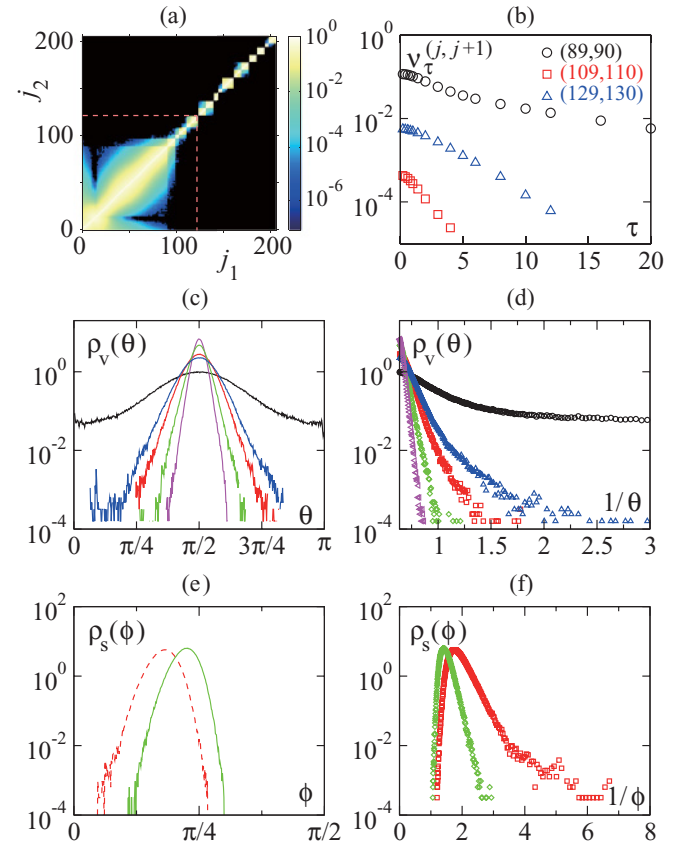


FIG. 30. (Color online) Hyperbolicity properties for the 2D KS equation. (a) Time fraction  $v_\tau^{(j_1, j_2)}$  of the DOS violation for arbitrary pairs with  $\tau = 0.2$ . The black color indicates  $v_\tau^{(j_1, j_2)} = 0$ , that is, hyperbolically isolated pairs. The red dashed lines indicate the threshold  $N_{\text{ph}} = 121$  between the physical and spurious modes. (b) Time fraction  $v_\tau^{(j, j+1)}$  of the DOS violation for pairs of neighboring Lyapunov exponents as a function of  $\tau$ . (c) Angle distributions  $\rho_v(\theta)$  for neighboring CLVs of indices (89, 90), (129, 130), (109, 110), (121, 122), and (137, 138) from outermost to innermost curve. Notice that they are not in order with respect to the index. (d)  $\rho_v(\theta)$  against  $1/\theta$ . The ordinate is averaged over both sides of the distribution. The order of the curves is the same as in (c) from upper right to lower left. (e) Angle distribution  $\rho_s(\phi)$  between the physical subspace ( $1 \leq j \leq N_{\text{ph}}$ ) and the spurious one ( $N_{\text{ph}} + 1 \leq j$ ) with  $N_{\text{ph}} = 121$  (green solid line). The red dashed line shows the angle distribution  $\rho_s(\phi)$  between the subspaces of indices  $1 \leq j \leq 109$  and  $110 \leq j$ . (f) The same plots as (e) but shown against  $1/\phi$  (green diamonds for the physical and spurious subspaces, and red squares for the other). Each color corresponds to the same index pair throughout in the panels (b)–(f).

in Fig. 28, which reproduces well the structure of the spurious region.

To locate exactly the threshold between the physical and spurious modes, one needs to measure the hyperbolicity properties as in all the other cases. Figure 30(a) shows the time fraction  $v_\tau^{(j_1, j_2)}$  of the DOS violation for arbitrary pairs  $(j_1, j_2)$ . Although internal connections are found for some neighboring steps of spurious modes, which are probably caused by mixing of several Fourier modes due to accidentally close values of the Lyapunov exponent [see Figs. 29(d)–29(f)], an unambiguous threshold is found at  $N_{\text{ph}} = 121$ , for which  $v_\tau^{(j_1, j_2)} = 0$  for all the pairs with  $j_1(j_2) \leq N_{\text{ph}} < j_2(j_1)$  even at the smallest  $\tau$  we used [red dashed line in Fig. 30(a)]. Varying  $\tau$  does not unravel the internal connections of spurious modes presumably, as  $v_\tau^{(j_1, j_2)}$  decays in the fastest case exponentially [Fig. 30(b)], whereas it would decay faster for a hyperbolically isolated pair [see Figs. 13(a) and 18(a)].

The same conclusion is reached from the angle distributions  $\rho_v(\theta)$  of the CLVs [Figs. 30(c) and 30(d)]. Pairs of CLVs for physical modes can take any angles and experience rather frequent tangencies, while the angle distribution for spurious pairs is peaked around  $\pi/2$  and decays quickly in the tail. A closer look at this tail reveals that hyperbolically isolated pairs, or those which fulfill the DOS, decay as  $\rho_v(\theta) \sim \exp(-\text{const}/\theta)$  or faster [two innermost plots in Fig. 30(d)] in contrast with the slower decays found for pairs of the physical modes (black circles and red squares) or the internally connected spurious modes (blue triangles). The hyperbolic decoupling at  $N_{\text{ph}} = 121$  is established by the same fast decay of the angle distribution  $\rho_s(\phi)$  between the two subspaces defined thereby [green full curve and diamonds in Figs. 30(e) and 30(f)]. Defining the threshold  $N_{\text{ph}}$  at a false value leads to a clearly slower decay in  $\rho_s(\phi)$  [red dashed curve and squares, obtained with the threshold corresponding to the red line and squares in Figs. 30(b)–30(d)]. In short, the hyperbolic decoupling between the physical manifold and the spurious modes takes place in the same way as for the 1D systems, with the peak wave numbers for the spurious modes distributed here in 2D Fourier space.

## VI. DISCUSSION

In the present paper, we have shown the hyperbolic decoupling of the tangent space in spatially extended dissipative systems into a finite set of  $N_{\text{ph}}$  physical modes characterizing all the physically relevant dynamics, and a remaining set of spurious modes, which represent trivial, exponentially decaying perturbations. Physical and spurious modes are characterized by the existence and absence, respectively, of tangencies between the associated CLVs. In contrast to physical modes, which are densely connected to each other through frequent tangencies, the spurious modes are hyperbolically isolated from all the physical modes, and therefore solely decay to zero without activating any physical modes. The existence or absence of tangencies between Lyapunov modes can be investigated both from the CLV angle distribution and the violation of DOS. One can also take into account linear combinations of physical or spurious modes by measuring the angle between the two subspaces spanned by the physical and spurious modes, respectively. This leads to the unambiguous

determination of the number of the physical modes,  $N_{\text{ph}}$ . We conjecture that this number corresponds to the minimal dimension of the inertial manifold. Moreover, we have shown that the hyperbolic decoupling between the physical and spurious modes takes place quite generically in dissipative systems, as we have found evidence in PDEs in one or higher spatial dimensions, as well as lattice systems with continuous or discrete time.

A few remarks about related earlier studies are in order. As already mentioned, the stepwise structure of the Lyapunov spectrum in the spurious region was already reported by Garnier and Wójcik for CGL amplitude turbulence, leading them to the conjecture that these are inactive Lyapunov exponents [36]. This is pertinent as we have revealed in the present study, but one should be reminded that the stepwise Lyapunov spectrum solely does *not* define or indicate the spurious modes. The steps do not form at a single well-defined threshold index: They are actually slightly inclined and get flatter and flatter as one goes deeper into the spurious region. As a matter of fact, the physical region typically extends to the first few steps of the spectrum: For the 1D KS system studied here the steps begin at  $j = 40$  but the spurious modes are from  $j = 44$ . This gap can be quite large; it is found to be 14 for the coupled tent maps studied in Sec. IV A. The formation of the steps is only a consequence of the sharp power spectrum and the choice of the boundary conditions.

In a different work, Ikeda and Matsumoto studied the projection of the dynamics onto Fourier modes or on the Gram-Schmidt vectors associated with the Lyapunov modes [41]. They measured in particular information-theoretic quantities and argued that information does not flow from a high wave number region to a lower wave number region. However, similarly to Lyapunov exponents, Gram-Schmidt vectors or Fourier modes alone cannot characterize the separation between physical and spurious modes, and thus cannot provide the exact index of the threshold. It is the CLVs that bear the true physical properties of tangent space and thus are able to define unambiguously the physical and spurious Lyapunov modes from their hyperbolicity properties.

Concerning the difference between the CLVs and the Gram-Schmidt vectors, while it is clear that properties directly linked to hyperbolicity such as angle distributions can only be captured by CLVs, one may formally study DOS using either CLVs or Gram-Schmidt vectors. However, clearly, the finite-time Lyapunov exponents defined using the two sets of vectors are *a priori* different for any finite times. Indeed, although these two definitions seem to give qualitatively similar results [42], it remains true that the mathematical connection to hyperbolicity is only proved for CLVs [30,31]. Thus, in the absence of a detailed study on this point, one cannot avoid computing CLVs for drawing any firm conclusion on hyperbolicity properties of dynamical systems.

We should also mention that all the angle distributions and the finite time Lyapunov exponents used for the determination of DOS are not invariant against coordinate transformations [43]. The splitting, however, between physical and spurious modes is coordinate independent because by smooth transformations a nonzero angle cannot be made to vanish and vice versa. Furthermore, the type of the essential singularity found in the angle distribution of critical pairs is invariant

against smooth transformations of the coordinates, as can be seen by considering how the angles are transformed with the coordinates. A simple example is provided by the two versions of the KS equations (1) and (16), which are connected by a linear transformation [40]. These considerations further emphasize the generality of our results.

Pursuing our conjecture that physical modes form the local approximation of the inertial manifold, it is crucial to seek a connection between CLVs and phase-space properties, and in particular to find a way to construct the inertial manifold using information of the physical CLVs. A straightforward construction is a manifold locally defined at each point of the trajectory by the physical CLVs, but strictly speaking, one also has to consider the nonlinear growth of finite-size perturbations, which is obviously not captured by Lyapunov analysis. Because of this, it is still, in principle, possible to consider a system in which hyperbolically isolated modes correspond to active degrees of freedom, such as a lattice of uncoupled hyperbolic maps as a trivial instance. However, given that the generic systems we studied are by no means hyperbolic, it is unlikely that that type of decoupling has any relation to the hyperbolic decoupling studied in the present paper.

Our results are also important from a practical point of view. Since the physical properties of the PDEs at stake are carried by the physical modes, a faithful numerical integration needs to incorporate at least as many degrees of freedom as the physical modes. In other words, the number of the physical modes,  $N_{\text{ph}}$ , sets a lower bound for the spatial resolution of the simulations. Moreover, the extensivity of  $N_{\text{ph}}$  implies that measuring it in systems of moderate size suffices to have reliable estimates for arbitrarily large system sizes. Our results may also be useful for controlling spatiotemporal chaos, in particular, when determining the minimal number of constraints for full control of such a system. A possible application in this context would be the suppression of ventricular fibrillation, the major reason of sudden cardiac death, for which promising schemes have been proposed recently applying low amplitude electric

shocks over grids of points or lines [44]. The number of the physical modes would then help determine an appropriate grid resolution. Note, however, that, having no access to the basis constituting the inertial manifold, one may actually need more degrees of freedom or constraints than  $N_{\text{ph}}$  to achieve faithful simulations or full control of a dissipative system. It is therefore of both fundamental and practical importance to elucidate the structure of the inertial manifold in phase space in the line of the present study.

In summary, we have shown, using Lyapunov analysis and, in particular, CLVs, that the tangent space of spatially extended dissipative systems can be divided into two parts: a finite-dimensional manifold spanned by the physical modes bearing all the physical information and the remaining set of spurious, exponentially decaying modes. We have demonstrated that the spurious modes are hyperbolically separated from all the physical modes and hence satisfy DOS. The separation holds for any linear combination of the physical or spurious modes, as the minimal angle between the physical and spurious subspaces is bounded away from zero. The number of physical modes has been interpreted as the number of effective degrees of freedom needed to describe the dynamics. This leads to the conjecture that the physical modes constitute a local approximation of the inertial manifold. We hope that these results will trigger mathematical studies in order to put these issues on a more rigorous basis. It is also interesting to perform further numerical investigations of other dissipative systems such as the Navier-Stokes equation, for which no rigorous proof of the existence of an inertial manifold is known.

## ACKNOWLEDGMENTS

The authors thank S. Sasa for informing us of his unpublished work on the mode description of solutions of the KS equation [33]. We acknowledge stimulating discussions with P. Cvitanović, A. Pikovsky, A. Politi, and S. Sasa.

- 
- [1] M. C. Cross and P. C. Hohenberg, *Rev. Mod. Phys.* **65**, 851 (1993).
  - [2] Y. Kuramoto, *Chemical Oscillations, Waves, and Turbulence* (Springer-Verlag, Berlin, 1984; republished by Dover, New York, 2003).
  - [3] P. Constantin, C. Foias, B. Nicolaenko, and R. Temam, *Integral Manifolds and Inertial Manifolds for Dissipative Partial Differential Equations*, Applied Mathematics Sciences, No. 70 (Springer-Verlag, Berlin, 1988).
  - [4] C. Foias, G. R. Sell, and R. Temam, *J. Differ. Equations* **73**, 309 (1988).
  - [5] J. C. Robinson, *Chaos* **5**, 330 (1995).
  - [6] I. S. Aranson and L. Kramer, *Rev. Mod. Phys.* **74**, 99 (2002).
  - [7] C. Foias, B. Nicolaenko, G. R. Sell, and R. Temam, *J. Math. Pures Appl.* **67**, 197 (1988).
  - [8] J. C. Robinson, *Phys. Lett. A* **184**, 190 (1994).
  - [9] M. S. Jolly, R. Rosa, and R. Temam, *Adv. Differential Equations* **5**, 31 (2000).
  - [10] J. M. Ghidaglia and B. Héron, *Physica D* **28**, 282 (1987).
  - [11] C. R. Doering, J. D. Gibbon, D. D. Holm, and B. Nicolaenko, *Nonlinearity* **1**, 279 (1988).
  - [12] D. Ruelle, *Commun. Math. Phys.* **87**, 287 (1982).
  - [13] P. Manneville, in *Macroscopic Modelling of Turbulent Flows*, Lecture Notes in Physics, Vol. 230, edited by U. Frisch *et al.* (Springer-Verlag, Berlin, 1985), p. 319.
  - [14] S. Tajima and H. S. Greenside, *Phys. Rev. E* **66**, 017205 (2002).
  - [15] L. Keefe, *Phys. Lett. A* **140**, 317 (1989).
  - [16] R. Livi, A. Politi, and S. Ruffo, *J. Phys. A: Math. Gen.* **19**, 2033 (1986).
  - [17] P. Grassberger, *Phys. Scr.* **40**, 346 (1989).
  - [18] P. Cvitanović, R. Artuso, R. Mainieri, G. Tanner, and G. Vattay, *Chaos: Classical and Quantum* (Niels Bohr Institute, Copenhagen, 2009).
  - [19] Y. Lan and P. Cvitanović, *Phys. Rev. E* **78**, 026208 (2008).
  - [20] P. Cvitanović, R. L. Davidchack, and E. Siminos, *SIAM J. Appl. Dyn. Syst.* **9**, 1 (2010).
  - [21] H.-I. Yang, K. A. Takeuchi, F. Ginelli, H. Chaté, and G. Radons, *Phys. Rev. Lett.* **102**, 074102 (2009).

- [22] J.-P. Eckmann and D. Ruelle, *Rev. Mod. Phys.* **57**, 617 (1985).
- [23] I. Shimada and T. Nagashima, *Prog. Theor. Phys.* **61**, 1605 (1979).
- [24] G. Benettin, L. Galgani, A. Giorgilli, and J.-M. Strelcyn, *Meccanica* **15**, 21 (1980).
- [25] F. Ginelli, P. Poggi, A. Turchi, H. Chaté, R. Livi, and A. Politi, *Phys. Rev. Lett.* **99**, 130601 (2007).
- [26] P. V. Kuptsov and S. P. Kuznetsov, *Phys. Rev. E* **80**, 016205 (2009).
- [27] Å. Björck and G. H. Golub, *Math. Comput.* **27**, 579 (1973).
- [28] A. V. Knyazev and M. E. Argentati, *SIAM J. Sci. Comput.* **23**, 2008 (2002).
- [29] Computation of the subspace angle  $\phi$  using sine instead of cosine was also formulated [27,28], which offers better accuracy in estimating small angles. Such an accuracy is, however, not necessary here, so we use the simpler formula given by Eq. (3).
- [30] C. Pugh, M. Shub, and A. Starkov, *Bull. Am. Math. Soc.* **41**, 1 (2004).
- [31] J. Bochi and M. Viana, *Ann. Math.* **161**, 1423 (2005).
- [32] H.-I. Yang and G. Radons, *Phys. Rev. Lett.* **100**, 024101 (2008).
- [33] S. Sasa (unpublished; private communication).
- [34] B. I. Shraiman, A. Pumir, W. van Saarloos, P. C. Hohenberg, H. Chaté, and M. Holen, *Physica D* **57**, 241 (1992).
- [35] H. Chaté, *Nonlinearity* **7**, 185 (1994).
- [36] N. B. Garnier and D. K. Wójcik, *Phys. Rev. Lett.* **96**, 114101 (2006).
- [37] H. Sakaguchi, *Prog. Theor. Phys.* **84**, 792 (1990).
- [38] P. V. Kuptsov and U. Parlitz, *Phys. Rev. E* **81**, 036214 (2010).
- [39] Moreover, in Ref. [38], it is not clear which definition of the finite-time Lyapunov exponents was used to study the DOS, namely, that using CLVs or Gram-Schmidt vectors. If the latter definition was used, there exists no mathematical argument that connects the order change in the finite-time exponents and their hyperbolicity properties.
- [40] The 1D KS equation (1) introduced in Sec. II is given in the differentiated form. One can derive it by applying  $\partial/\partial x$  to the 1D counterpart of Eq. (16).
- [41] K. Ikeda and K. Matsumoto, *J. Stat. Phys.* **44**, 955 (1986); *Phys. Rev. Lett.* **62**, 2265 (1989).
- [42] P. V. Kuptsov and A. Politi, *Phys. Rev. Lett.* **107**, 114101 (2011).
- [43] H.-I. Yang and G. Radons, *Phys. Rev. E* **82**, 046204 (2010).
- [44] See for example W.-J. Rappel, F. Fenton, and A. Karma, *Phys. Rev. Lett.* **83**, 456 (1999); S. Sinha, A. Pande, and R. Pandit, *ibid.* **86**, 3678 (2001); the scheme was originally introduced in H. Gang and Q. Zhilin, *ibid.* **72**, 68 (1994).